

FULL PAPER

Open Access



# Configuration and structure of the Philippine Sea Plate off Boso, Japan: constraints on the shallow subduction kinematics, seismicity, and slow slip events

Aki Ito<sup>1\*</sup> , Takashi Tonegawa<sup>1</sup>, Naoki Uchida<sup>2</sup>, Yojiro Yamamoto<sup>1</sup>, Daisuke Suetsugu<sup>1</sup>, Ryota Hino<sup>2</sup>, Hiroko Sugioka<sup>3</sup>, Koichiro Obana<sup>1</sup>, Kazuo Nakahigashi<sup>4</sup> and Masanao Shinohara<sup>5</sup>

## Abstract

We applied tomographic inversion and receiver function analysis to seismic data from ocean-bottom seismometers and land-based stations to understand the structure and its relationship with slow slip events off Boso, Japan. First, we delineated the upper boundary of the Philippine Sea Plate based on both the velocity structure and the locations of the low-angle thrust-faulting earthquakes. The upper boundary of the Philippine Sea Plate is distorted upward by a few kilometers between 140.5 and 141.0°E. We also determined the eastern edge of the Philippine Sea Plate based on the delineated upper boundary and the results of the receiver function analysis. The eastern edge has a northwest–southeast trend between the triple junction and 141.6°E, which changes to a north–south trend north of 34.7°N. The change in the subduction direction at 1–3 Ma might have resulted in the inflection of the eastern edge of the subducted Philippine Sea Plate. Second, we compared the subduction zone structure and hypocenter locations and the area of the Boso slow slip events. Most of the low-angle thrust-faulting earthquakes identified in this study occurred outside the areas of recurrent Boso slow slip events, which indicates that the slow slip area and regular low-angle thrust earthquakes are spatially separated in the offshore area. In addition, the slow slip areas are located only at the contact zone between the crustal parts of the North American Plate and the subducting Philippine Sea Plate. The localization of the slow slip events in the crust–crust contact zone off Boso is examined for the first time in this study. Finally, we detected a relatively low-velocity region in the mantle of the Philippine Sea Plate. The low-velocity mantle can be interpreted as serpentinized peridotite, which is also found in the Philippine Sea Plate prior to subduction. The serpentinized peridotite zone remains after the subduction of the Philippine Sea Plate and is likely distributed over a wide area along the subducted slab.

**Keywords:** Subducted Philippine Sea Plate, Slow slip events, Seismic structure from amphibious array, Off-Boso area

\*Correspondence: iaki@jamstec.go.jp

<sup>1</sup> Research Institute for Marine Geodynamics, Japan Agency of Marine-  
Earth Science and Technology, 2-15 Natsushima-cho, Yokosuka,  
Kanagawa 237-0061, Japan

Full list of author information is available at the end of the article

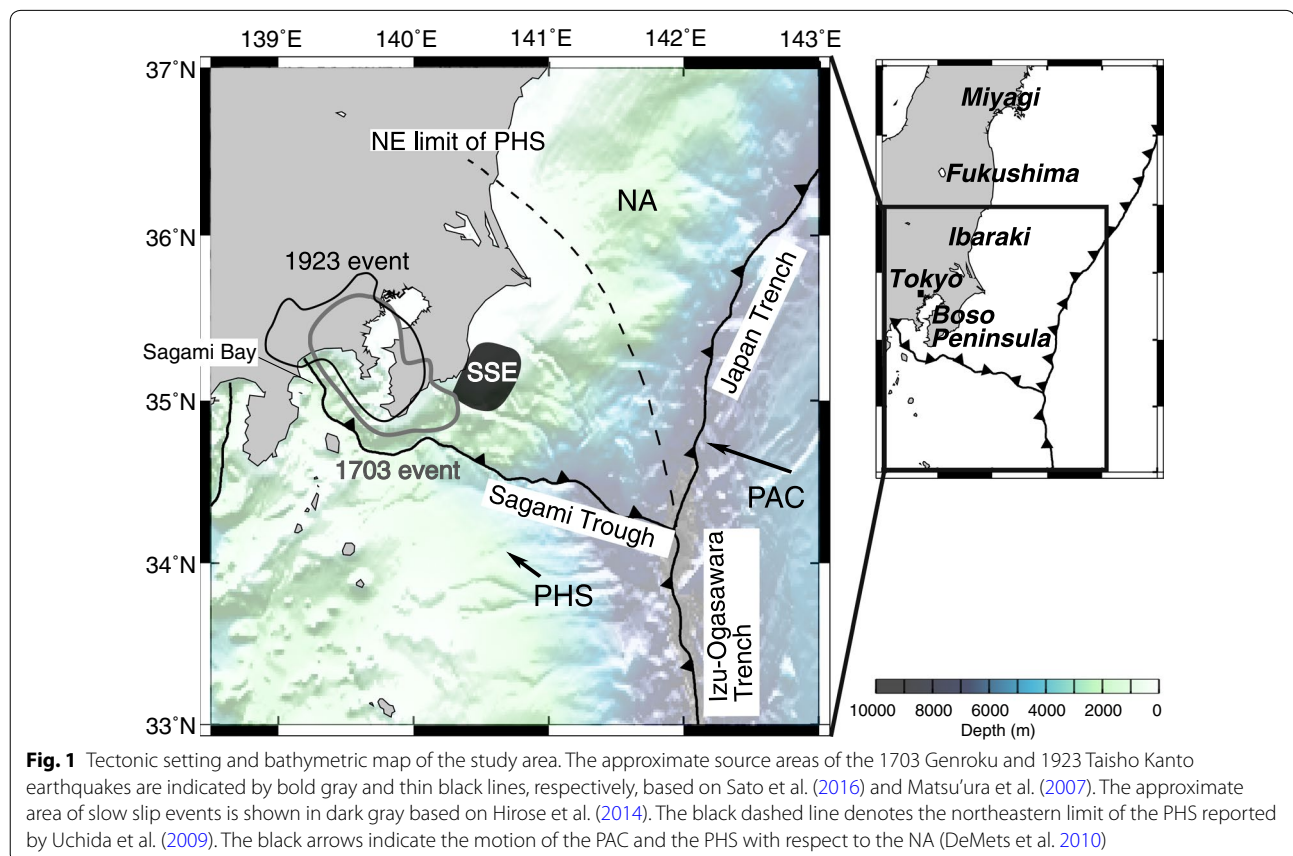
## Introduction

The off-Boso area, which is located in central Japan, has a very complicated tectonic setting, as shown in Fig. 1. Three tectonic plates overlap in this region. In the eastern part of the region, the Pacific Plate (PAC) with an age of 130–140 Myr (Müller et al. 2008) is subducting westward at the Japan Trench beneath the North American Plate (NA) with a relative speed of 8.3 cm/a (DeMets et al. 2010). In the southern part of the region, the Philippine Sea Plate (PHS) with an age of 45 Myr (e.g., Ishizuka et al. 2011) is subducting northwestward beneath the NA at the Sagami Trough with a relative speed of 3.0–3.8 cm/a (e.g., Seno and Maruyama 1984; DeMets et al. 2010). The subducted PHS overrides the PAC (e.g., Ishida 1992; Hori 2006), and its northeastern limit has been defined based on the slip directions of the interplate earthquakes (Uchida et al. 2009). The PHS subducted northward from 15 Ma to 1–3 Ma, when it changed the subduction direction to northeastward (e.g., Yamaji 2000; Kamata 2003; Takahashi 2006).

Various seismic and geodetic activities associated with PHS subduction have been observed around the off-Boso area. Large earthquakes have repeatedly occurred in the area (e.g., the Mw7.9 Taisho Kanto earthquake in 1923

and the Mw7.9–8.2 Genroku Kanto earthquake in 1703) and have resulted in severe damage in central Japan, which includes the current Tokyo metropolitan area (Fig. 1). Both the Taisho and Genroku earthquakes were thrust events associated with the subduction of the PHS under the overriding NA plate (e.g., Ando 1971; Matsuda et al. 1978; Matsu'ura et al. 1980, 2007; Takemura 1994; Wald and Somerville 1995; Namegaya et al. 2011; Sato et al. 2016).

In addition to regular earthquakes, slow slip events (SSEs) occur with an average interval of approximately 6 years at the interface between the PHS and the NA (e.g., Sagiya 2004; Ozawa et al. 2007; Hirose et al. 2014; Ozawa 2014) beneath the off-Boso area (Fig. 1). Two SSEs in 2007 and 2011 have been studied in detail using tiltmeters and a nationwide global navigation satellite system (GNSS) network (Hirose et al. 2012, 2014), which indicated that the SSEs lasted for a few weeks and had moment magnitudes of 6.4–6.6. The Boso SSEs may be related to the seismic activity of small regular earthquakes. The regular earthquake area and the slow slip area do not overlap beneath the Boso Peninsula (e.g., Hirose et al. 2012, 2014). However, the segregation of regular earthquakes and SSEs is not clear in the offshore



area because the hypocenter locations of regular earthquakes offshore are not well constrained. The subduction zone structure may also be related to the occurrence of SSEs. SSEs in the Tokai region, 300 km west of the off-Boso area, are thought to only be located at contact zones between the crust of the overriding plate and the crust of subducting plate (e.g., Kodaira et al. 2004; Kato et al. 2010). Conversely, the relationship between SSEs and the subduction zone structure is unknown off Boso because a detailed three-dimensional structure of the region is not available.

Several offshore observations with ocean-bottom seismometers (OBSs) were made in the northern part of the off-Boso area (Shinohara et al. 2011, 2012) following the 2011 Tohoku-oki earthquake. In the southern part of the area, the Japan Agency for Marine–Earth Science and Technology (JAMSTEC) conducted earthquake observations for 1 year starting in March 2012 (Ito et al. 2017a, b). Even though Ito et al. (2017a) determined the hypocenter distribution and focal mechanisms of the earthquakes in the off-Boso area, they analyzed the earthquakes using a simplified velocity model, which was constructed based on the results of previous studies (Ito et al. 2005; Hino et al. 2009; Nakajima et al. 2009; Nakahigashi et al. 2012). Ito et al. (2017b) obtained the three-dimensional velocity structure off Boso by the tomographic inversion; however, they could not reliably determine the velocity structure near the coastline of the Boso Peninsula due to the small number of land-based stations in their study.

The number of stations and methods in this and previous studies (Ito et al. 2017a, b) is summarized in Table 1. In this study, we extended the studies of Ito et al. (2017a, b) in two ways. First, we increased the land-based data by three times compared to those used in Ito et al. (2017b) in the tomographic inversion to improve the spatial resolution of the velocity structure near the coastline, where SSEs have occurred in the past. The OBS data used in Ito et al. (2017b) were also analyzed in this study. Second, we determined the locations and focal mechanisms of the earthquakes more accurately than those estimated in Ito

et al. (2017a) using a tomographically determined velocity structure. In addition to these improvements, this study applied a receiver function (RF) analysis to the teleseismic *P* waveforms observed at the OBSs, from which seismic velocity discontinuities related to the plate interfaces were detected. The depth conversion was achieved using a three-dimensional velocity model obtained from the tomographic inversion.

The main subjects addressed in the present paper are (1) the shape of the upper boundary and the eastern edge of the PHS based on the velocity structure, the RF analysis, and the locations of the low-angle thrust-faulting earthquakes in the offshore area, where previous studies had not been resolved, and (2) the relationship between the area of the past SSEs and the velocity structure.

## Data

We analyzed seismic data from temporary OBS observations operated by JAMSTEC (Ito et al. 2017a, b) and the Earthquake Research Institute (ERI) of the University of Tokyo (Shinohara et al. 2011, 2012). Figure 2 shows the locations of the stations. The JAMSTEC OBSs included four broadband OBSs (BBOBSs) and 20 short-period OBSs (SPOBSs), which covered the southern part of the off-Boso area. The specifications and observational periods of the stations are summarized in Table 2. The detailed locations and information concerning each OBS station are given in Additional file 1: Tables S1, S2 and in Figure S1. One SPOBS (S15) was not analyzed due to an internal clock error. We analyzed the seismic signals obtained by the differential pressure gauges due to a problem with a seismic sensor in one of the BBOBSs (BB3). The ERI OBSs included 50 long-term OBSs (LTOBSs) that covered the northern part of the off-Boso area. In addition to the data from the OBSs, we used seismic data from 45 land-based stations and 3 cabled offshore stations operated by the National Research Institute for Earth Science and Disaster Resilience (NIED) (Okada et al. 2004). In Ito et al. (2017a, b), data from only 15 NIED stations were used (Table 1).

**Table 1** Specifications and observational periods of the stations

	Ito et al. (2017a)	Ito et al. (2017b)	This study
Number of OBS	74	74	74
Number of land station	15	15	48
Method	1. Hypocenter location using a simplified 3-D model 2. Focal mechanisms using a simplified 3-D model	1. Initial hypocenter location using 1-D model 2. Seismic tomography	1. Initial hypocenter location using 1-D model 2. Seismic tomography 3. Focal mechanisms using the 3-D velocity structure by tomography 4. RF analysis

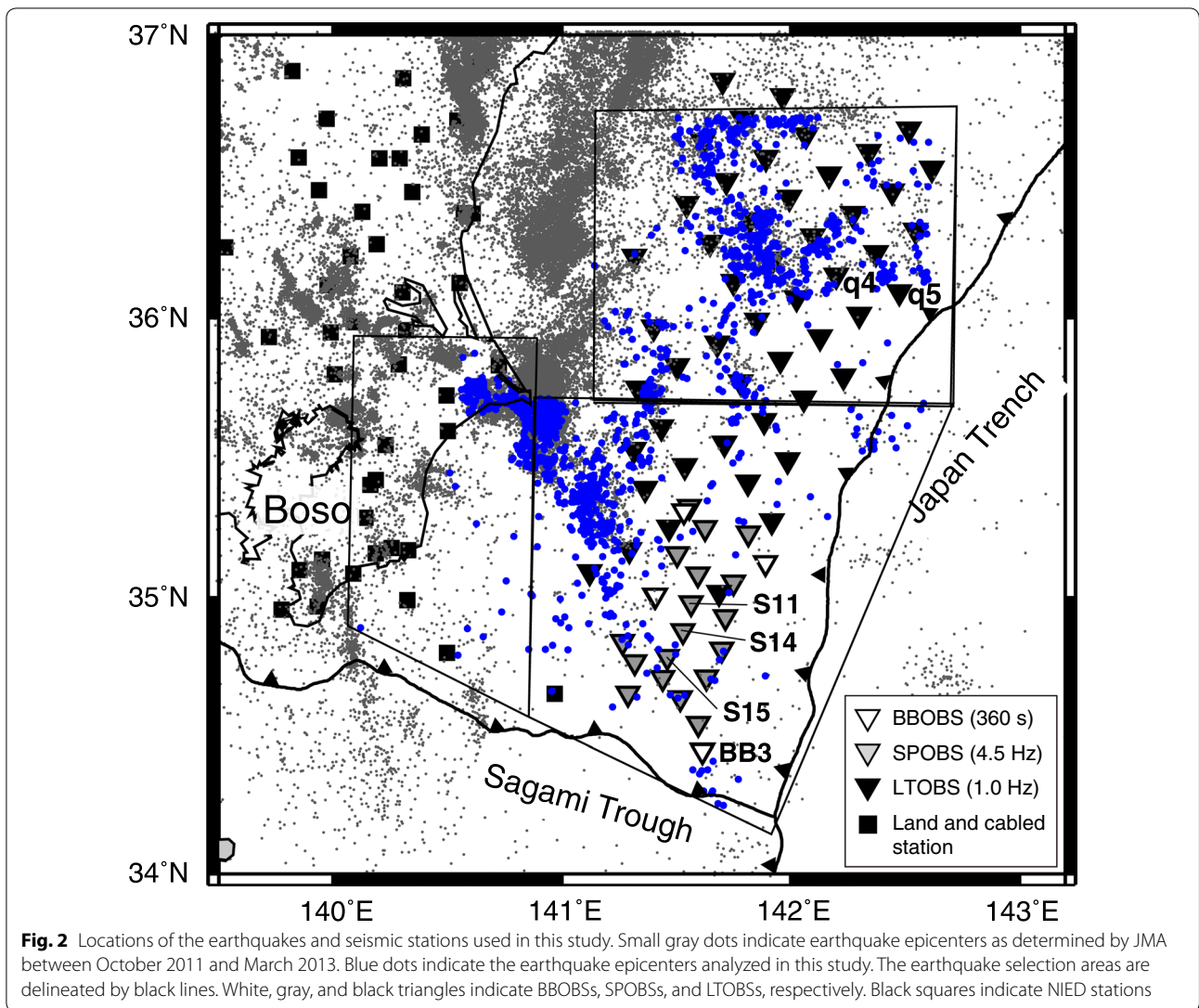


**Fig. 2** Locations of the earthquakes and seismic stations used in this study. Small gray dots indicate earthquake epicenters as determined by JMA between October 2011 and March 2013. Blue dots indicate the earthquake epicenters analyzed in this study. The earthquake selection areas are delineated by black lines. White, gray, and black triangles indicate BBOBSs, SPOBSs, and LTOBSs, respectively. Black squares indicate NIED stations

**Table 2 Specifications and observational periods of the stations**

Station	Natural frequency of sensor	Sampling rate (Hz)	Number of stations	Observation period
BBOBS	360 s	200	4	Mar. 2012–Mar 2013
SPOBS	4.5 Hz	100	7	Mar. 2012–Mar 2013
SPOBS	4.5 Hz	100	10	May 2012–Mar 2013
SPOBS	4.5 Hz	100	3	Dec 2012–Mar 2013
LTOBS	1 Hz	200	15	Oct 2011–Aug 2012
LTOBS	1 Hz	200	35	Apr 2012–Nov 2012
Land	1, 3, 5 Hz	100	48	

We analyzed 1430 local earthquakes (the blue dots in Fig. 2) with magnitudes of 1.1–6.3 that occurred from October 2011 to March 2013 in the Japan Meteorological

Agency (JMA) catalog to examine the seismic activity and velocity structure. A histogram of the earthquake magnitudes is given in Additional file 1: Figure S2, showing that most of earthquakes analyzed in this study have magnitudes greater than 2.0. We selected the earthquakes for which at least 10 arrival data were available within three regions that are indicated by the black lines in Fig. 2. We manually picked the *P*- and *S*-wave onset times from the vertical and horizontal components of the OBS data, respectively. The picking accuracies for *P*- and *S*-wave arrival times are 0.1 and 0.2 s, respectively. In addition, we recorded the polarity of the *P*-wave first motions when available. Example of seismic record for a local earthquake is shown in Additional file 1: Figure S3.

We collected the arrival data of the *P*- and *S*-waves and the *P*-wave first motion data from a catalog provided by JMA for the land-based and cabled offshore stations.

The total numbers of *P*- and *S*-wave arrivals used for the initial hypocenter relocation were 47,972 and 27,286, respectively. Of these data, 47,293 and 25,184 data for the *P*- and *S*-waves, respectively, were used as the absolute travel times for the tomographic inversion. A total of 120,455 and 57,817 data for the *P*- and *S*-waves, respectively, were used as the differential travel times in the tomographic inversion.

For the RF analysis, teleseismic *P*-waves were collected from seismic records observed at the OBSs. We selected events from the United States Geological Survey (USGS) catalog with the criteria of epicentral distances of 30–90° and magnitudes of >5.5 (Fig. 3). We hand-picked the *P* arrival times in the frequency band of 0.5–2 Hz. We list the number of events for the RF analysis in Additional file 1: Tables S1 and S2. We applied the RF analysis to the records obtained by 64 of the 74 total OBS stations. We selected the OBS stations for which at least 10 events could be picked manually and the horizontal orientation

of the OBS could be determined (see “RF analyses” section). The number of events used at each OBS was 10–68.

## Method

### Seismic activity and velocity structure

First, we obtained the initial hypocenters for the tomographic inversion using the NonLinLoc software (Lomax et al. 2000) and a one-dimensional JMA2001 velocity model (Ueno et al. 2002). Next, the three-dimensional *P*- and *S*-velocity structures and earthquake locations were determined using tomoDD (Zhang and Thurber 2003). We evaluated the spatial resolution of the velocity model on both the recovered checkerboard resolution test pattern (Spakman and Nolet 1988) and using the derivative weight sum (DWS) values (Thurber and Eberhart-Phillips 1999). The above-mentioned analysis procedure was basically the same as that used by Ito et al. (2017b).

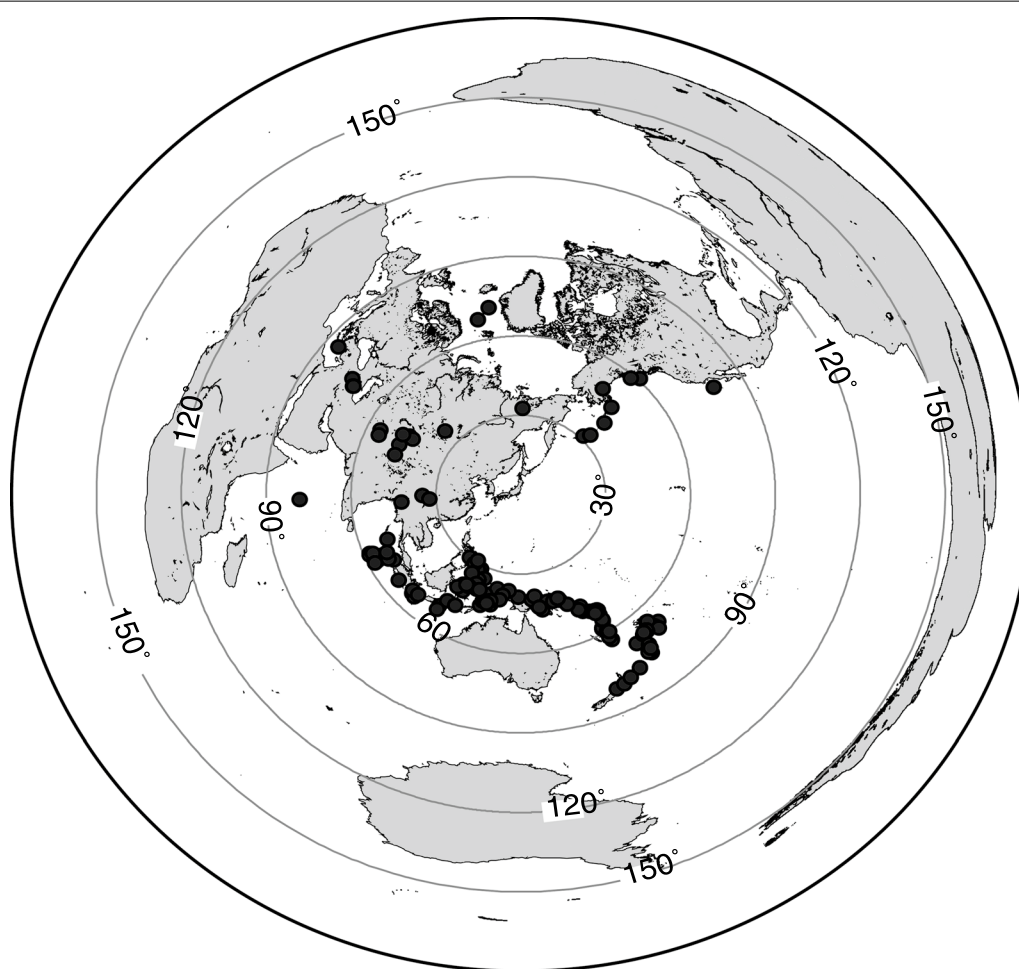


**Fig. 3** Locations of the earthquakes used in the RF analysis. The center of the map is the off-Boso area. Dark gray circles indicate earthquake epicenters from the USGS catalog

The model space for the tomography was expressed using orthogonal coordinates, as shown in Fig. 4. The horizontal grids were set at intervals of 20 km, which was comparable to the average spacing of the OBS stations, and the vertical grid was set at intervals of 5 km down to 50 km.

After the tomographic inversion, the FOCMEC code (Snoke 2003) was used to determine the focal mechanisms from the *P*-wave polarity data. We used the hypocenter locations, take-off angles, and azimuths obtained by tomoDD.

**RF analyses**

It is necessary to determine the horizontal orientations of the OBSs to obtain a radial-component seismogram for the RF analysis. We estimated the orientations from an early part of the *P*-wave first motion of teleseismic events

(e.g., Nakano et al. 2012) at frequencies of 0.02–0.05 Hz and 0.03–0.1 Hz for the BBOBSs and LTOBSs, respectively. The orientations can be estimated by maximizing the correlation between the *P* waveform rotated from two horizontal-component seismograms and the *P* waveform on the vertical-component seismogram. The orientation of one LTOBS (q5) was not obtained due to low-quality data. For the SPOBSs, which were equipped with a higher natural frequency sensor than the BBOBSs and LTOBSs, we estimated the orientations using the *T*-wave particle motion of the near-field events (Shan et al. 2012; Toneygawa et al. 2017) because we could not find a reliable orientation for the SPOBSs using teleseismic *P*-waves. The *T*-waves are useful for the SPOBSs because the horizontal particle motion of a *T* wave is nearly linear and directed toward an epicenter. The estimated orientation with this method included an arbitrary 180°. Two

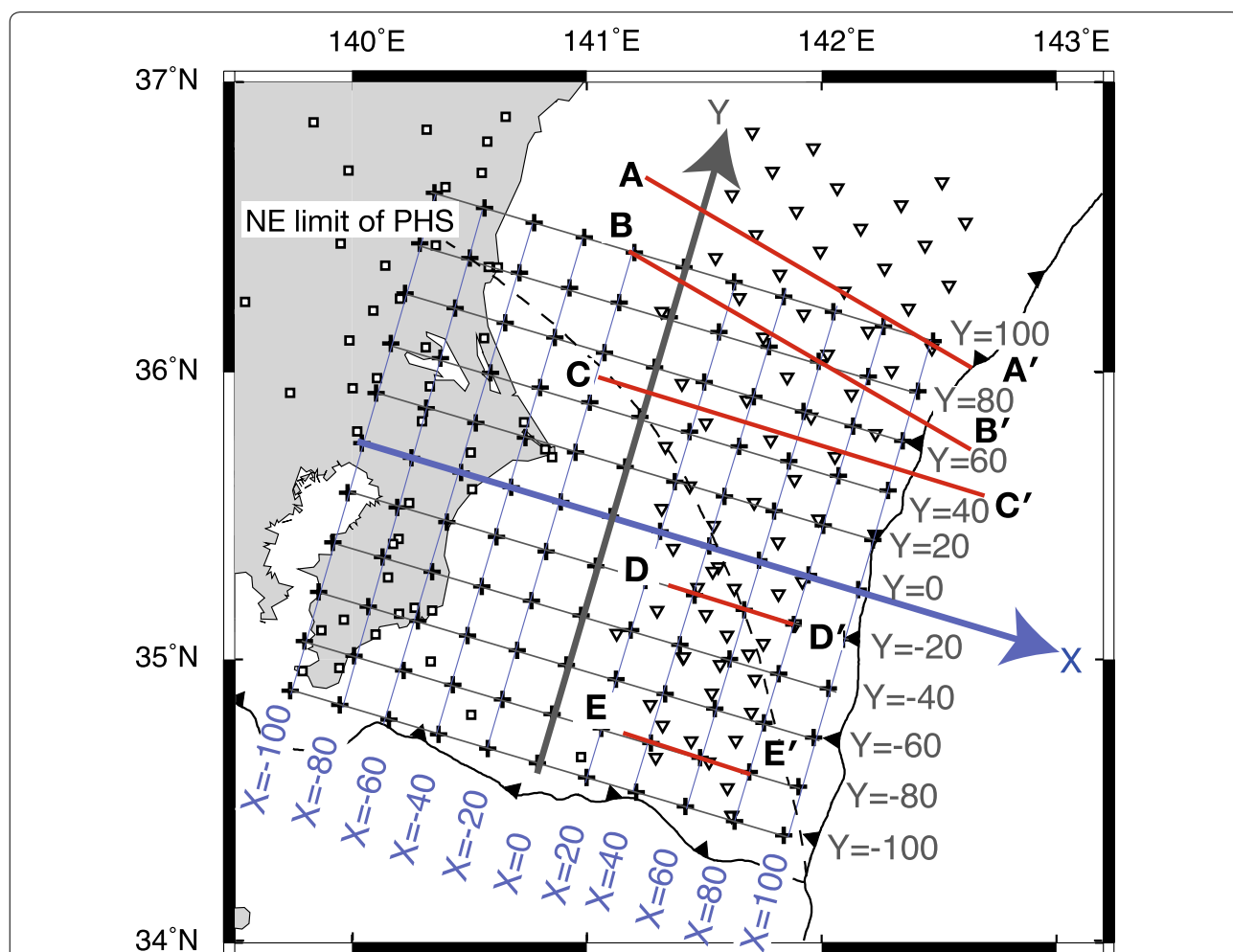


**Fig. 4** Configuration of the grid nodes during the tomographic inversions and the projected lines for the stacked RF images. The crosses represent the locations of velocity nodes in the horizontal section. The triangles and squares indicate stations. Lines A–A′, B–B′, C–C′, D–D′, and E–E′ define the locations of the depth-domain RFs

SPOBSs (S11 and S14) were not used for the RF analysis because the estimated orientation varied depending on the earthquake and we could not obtain a reliable value.

The ray paths of major seismic phases isolated from teleseismic *P* wave for seafloor observation are shown in Additional file 1: Figure S4. The RFs were calculated through a spectral division of the radial components by the vertical components with a water level of 0.001 (e.g., Langston 1977, 1979). We used a time window from  $-2$  to  $3$  s from the picked *P* arrival times in the vertical component to avoid contamination of water reverberation in the deconvolution (Tonegawa et al. 2018) and applied a cosine taper of 10% of the time window. The time window of the radial component was from  $-2$  s to  $14$  s from the picked *P* arrival times. We applied a bandpass filter of  $0.5$ – $2.0$  Hz to the RFs.

We calculated the synthetic RFs with reflectivity method (Kennett 1983, 2001) at one OBS (q4) to examine

the appropriate time window in the vertical component for the deconvolution. Figure 5b shows the synthetic waveforms of the vertical and radial components from a teleseismic event with a slowness of  $0.062$  s/km. These waveforms were calculated using a one-dimensional velocity and density model that was simplified from the three-dimensional velocity structure obtained by the tomographic inversion (Fig. 5a) at station q4. The density was estimated from  $V_p$  using an empirical relationship (Brocher 2005). Figure 5c shows the two synthetic RFs obtained by deconvolution using vertical-component seismograms with time windows from  $-2$  to  $20$  s and from  $-2$  to  $3$  s. The RF using a time window from  $-2$  to  $20$  s (the top panel in Fig. 5c) is noisier compared to that using a time window from  $-2$  to  $3$  s (the bottom panel in Fig. 5c) because water reverberation contaminates the RF for the case of the time window from  $-2$  to  $20$  s. In the case of the time window from  $-2$  to  $3$  s, the

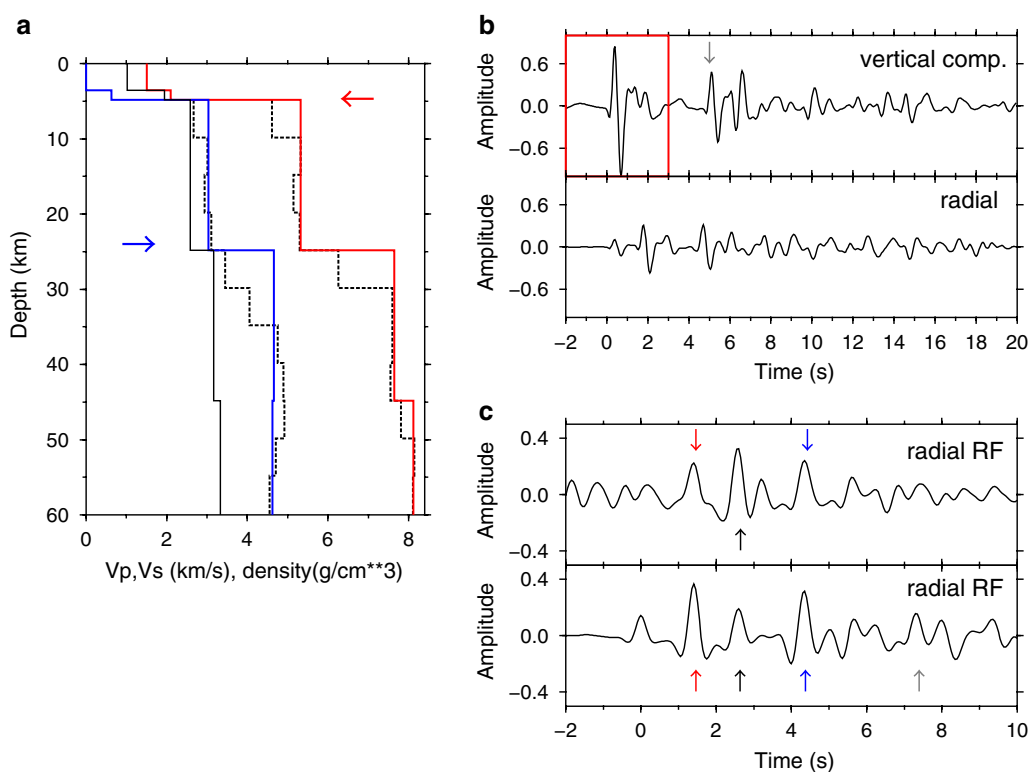


**Fig. 5** Synthetic test of two time windows in the vertical component for the deconvolution. **a** Velocity and density models for calculating the synthetic RFs. The dashed lines indicate the *P*- and *S*-wave velocity models based on the results of the tomographic inversion at station q4. The red, blue, and black lines represent the assumed *P*-wave, *S*-wave, and density models derived from the original model (the dashed lines). The red and blue arrows show the top of the basement and the Moho of the PAC, respectively. **b** Synthetic waveforms in the (top) vertical and (bottom) radial components for a slowness of  $0.062$  s/km and at a frequency band of  $0.5$ – $2.0$  Hz. The waveform in the red box was used for the deconvolution to calculate the RF at the bottom of panel (c). The peak indicated by the gray arrow is produced by *P<sub>w</sub>P* (reflected-*P* wave from sea surface). **c** Radial RFs using (top) a time window from  $-2$  to  $20$  s in the vertical component and (bottom) a time window from  $-2$  to  $3$  s in the vertical component. The peaks indicated by the red and blue arrows are produced by the subseafloor boundaries indicated by the top of the basement and the Moho of the PAC, respectively, which are indicated by the red and blue arrows in **a**. The peak indicated by the black arrow is produced by *P<sub>s</sub>S<sub>s</sub>* (multiple reflections in the sediment). The peak indicated by the gray arrow is produced by *P<sub>w</sub>P<sub>s</sub>* (multiple reflections caused by a seawater layer)

RF amplitudes associated with the real subseafloor velocity boundaries, such as the top of the basement and the Moho of the PAC, can be clearly seen compared to those in the case of the time window from  $-2$  to  $20$  s. Therefore, we decided to use the time window from  $-2$  to  $3$  s in the vertical component for the deconvolution.

To convert from a time-domain RF to a depth-domain RF, we employed the three-dimensional velocity model obtained in this study. Prior to the conversion from the time-domain to the depth-domain, we time-shifted the time-domain RF by  $T_{ps}$  (the differential travel time of the  $P$ - and  $S$ -waves in the shallow sediments above the Cretaceous layer) because the tomographic model was obtained from travel-time data that were corrected for the shallow sediments. Therefore, the  $P_s$  amplitudes at  $0$  km of the resulting depth-domain RFs are the converted phase at the top of the Cretaceous sediment and the functions are plotted from the depth of the top of the Cretaceous sediment, which can be estimated from  $T_{ps}$  and  $V_p/V_s$  in the shallow sediments, in the RF imaging. Methods to obtain parameters with respect to shallow sediments such as  $T_{ps}$  and  $V_p/V_s$  are described in Ito et al. (2017b). For the RF imaging, a common conversion-point stacking technique (e.g., Yamauchi et al. 2003; Toneyama et al. 2005) was used with a cell size of  $1 \text{ km} \times 1 \text{ km}$  in the horizontal and depth directions.

## Results

### Low-angle thrust-faulting earthquakes

We determined the hypocenter locations of 1302 earthquakes with errors of less than  $3$  km in the horizontal direction and  $4$  km in the depth direction by the tomographic inversion (Additional file 1: Figure S5). We obtained the focal mechanisms solutions for 488 earthquakes, and the location errors of the earthquakes are less than  $2.9$  km and  $3.3$  km in the horizontal and vertical directions, respectively. We selected focal mechanism solutions in which the number of inconsistent polarity data was less than 20% of the total polarity data. The focal mechanisms of 268, 162, and 22 earthquakes were reverse, normal, and strike-slip faulting types, respectively, following the classification of Frohlich (1992).

Figure 6a shows the distribution of 214 low-angle thrust-faulting earthquakes, which are defined as reverse faulting earthquakes that have a nodal plane dip angle of less than  $35^\circ$ . Of these, we indicate the earthquakes associated with PAC and PHS subduction with light blue and magenta, respectively, as described below. A total of 156 earthquakes had focal mechanisms consistent with PAC subduction (E–W). These events have focal depths within  $6$  km of the upper boundary of the PAC proposed by Nakajima et al. (2009) (the brown line in Fig. 6). In the part shallower than the PAC upper boundary by more

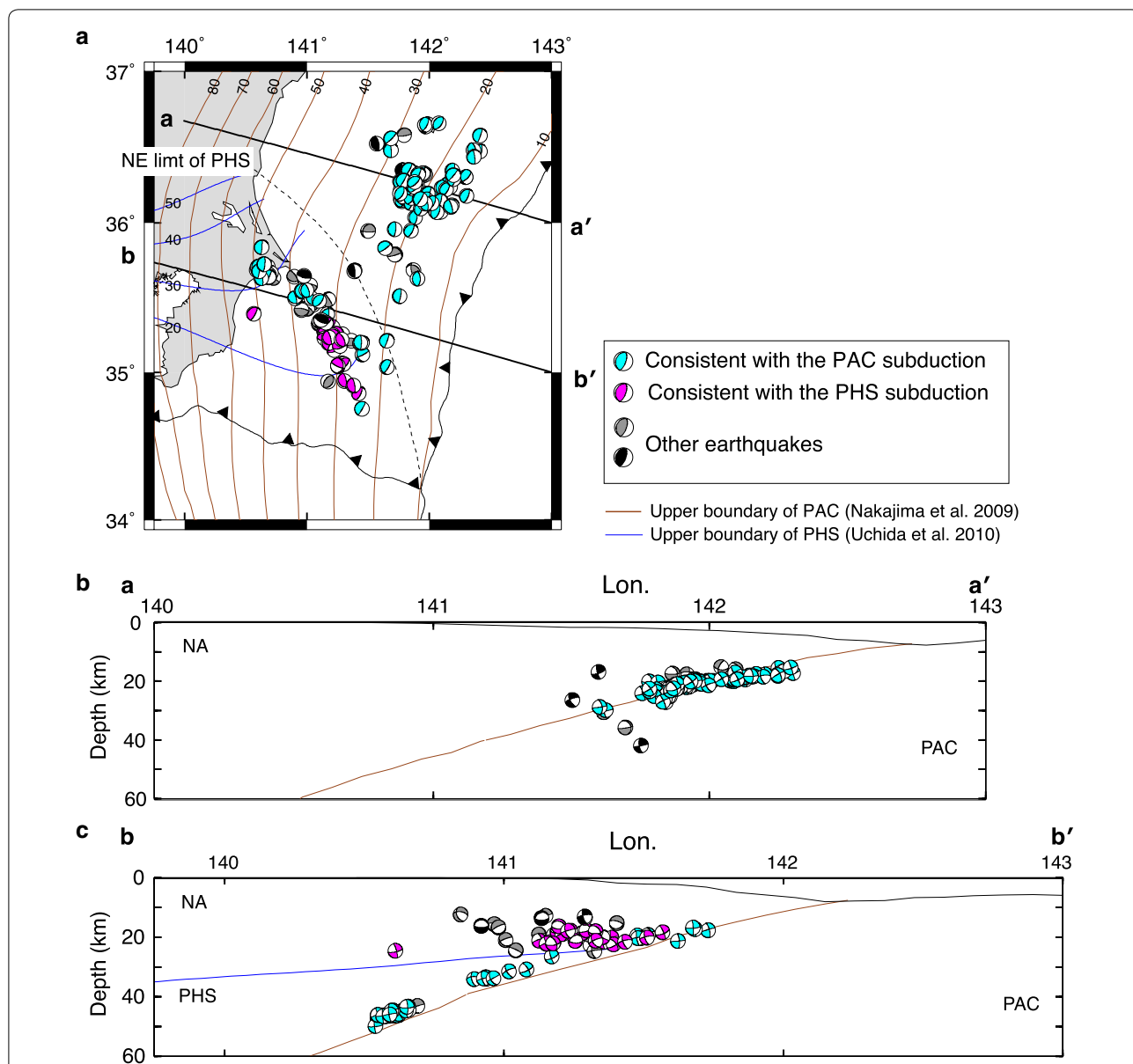
than  $6$  km, 28 earthquakes had focal mechanisms consistent with PHS subduction (NW–SE) or the PHS dip direction (N–S), which we interpreted as earthquakes associated with PHS subduction. The rest of the low-angle thrust-faulting earthquakes are shown in black and gray; the focal mechanisms shown in gray have nodal planes inconsistent with the PAC and PHS subduction directions, and those shown in black are not thought to be interplate earthquakes due to their focal depths.

Figure 6b and c shows depth profiles of the focal mechanisms along the lines a–a' and b–b' in Fig. 6a. In the north to northeastern limit of the PHS proposed by Uchida et al. (2009), the focal mechanisms are plotted in the depth profile along the line a–a' (Fig. 6b). Most of the earthquakes are associated with PAC subduction and their focal depths are consistent with the PAC geometry proposed by Nakajima et al. (2009). In the south to northeastern limit of the PHS, the focal mechanisms are plotted in the depth profile along the line b–b' in Fig. 6c. The earthquakes associated with PHS subduction are shallower by  $3$ – $6$  km than the PHS upper boundary proposed by Uchida et al. (2010).

### Three-dimensional velocity structure

The root mean square of the total travel-time residuals decreased from  $0.49$  s to  $0.25$  s after 26 tomographic inversion iterations. We show the W–E and S–N depth profiles of the tomographic images in Figs. 7 and 8, respectively. The unresolved areas of  $DWS < 4000$  for the  $P$ -wave model and of  $DWS < 1000$  for the  $S$ -wave model are masked. The spatial patterns for the wavelengths greater than  $40$  km in the horizontal and  $10$  km in the vertical directions were robust for the  $P$ - and  $S$ -waves at depths of  $10$ – $30$  km in nearly the entire studied region. The velocity structure north of  $Y = -20$  km has a higher resolution than that of Ito et al. (2017b) at depths of  $> 20$  km.

A region with  $V_p$  and  $V_s$  values of  $7.5$ – $8.5$  km/s and  $4.0$ – $4.8$  km/s, respectively, was imaged beneath numerous low-angle thrust-faulting earthquakes denoted by red circles and the upper boundary of the PAC in Nakajima et al. (2009). From its location and velocity values, this region likely corresponds to the mantle part of the PAC (“PaM” in the figure). Above the PAC, a region with  $V_p$  and  $V_s$  values of  $< 7.0$  km/s and  $< 4.0$  km/s, respectively, was imaged at depths of  $< 25$  km in the northern part of the studied region (north of  $Y = 40$  km in Fig. 7). This is likely the crustal part of the NA (“NaC” in the figure) because refraction studies suggest that the crust of the NA has  $V_p$  values of  $< 7.0$  km/s from the off-Ibaraki to off-Miyagi areas (e.g., Miura et al. 2003; Ito et al. 2005). Beneath the crust of the NA, a region of  $V_p$  and  $V_s$  values of  $7.0$ – $8.0$  km/s and  $4.5$  km/s, respectively, was imaged.



**Fig. 6** Distribution and focal mechanisms of low-angle thrust-faulting earthquakes. The light blue and magenta beach balls indicate earthquakes associated with PAC and PHS subduction, respectively. The focal mechanisms, shown in black and gray, are earthquakes inconsistent with subduction. **a** Lines a–a’ and b–b’ define the projected lines onto the cross-sections. The brown and blue lines indicate the depths of the upper boundaries of the PAC (Nakajima et al. 2009) and PHS (Uchida et al. 2010), respectively. **b** Cross-section along line a–a’. The focal mechanisms north of the northeastern limit of the PHS are plotted. **c** Cross-section along line b–b’. The focal mechanisms south of the northeastern limit of the PHS are plotted

This region may represent the mantle part of the NA (“NaM” in the figure).

In the south of the studied region, the tomographic image shows a region with a  $V_p$  value of 7.5–8.0 km/s above the PAC. This area was observed at depths of 25–30 km at  $Y = -40$  km and  $Y = -60$  km in Fig. 7. A region with a  $V_s$  value of 4.0 km/s in the S-wave model was also observed but was unclear owing to the relative

insufficiency of the S-wave data. The  $V_p$  value is comparable to that in the mantle of the PHS as determined by tomographic studies on land ( $V_p = 7.5\text{--}8.2$  km/s) at depths greater than 30 km (Matsubara et al. 2005; Nakajima et al. 2009). Therefore, this region may correspond to the mantle part of the PHS (“PhM” in the figure). Around the mantle part of the PHS, we observed a region with  $V_p$  and  $V_s$  values of 6.5–7.0 km/s and

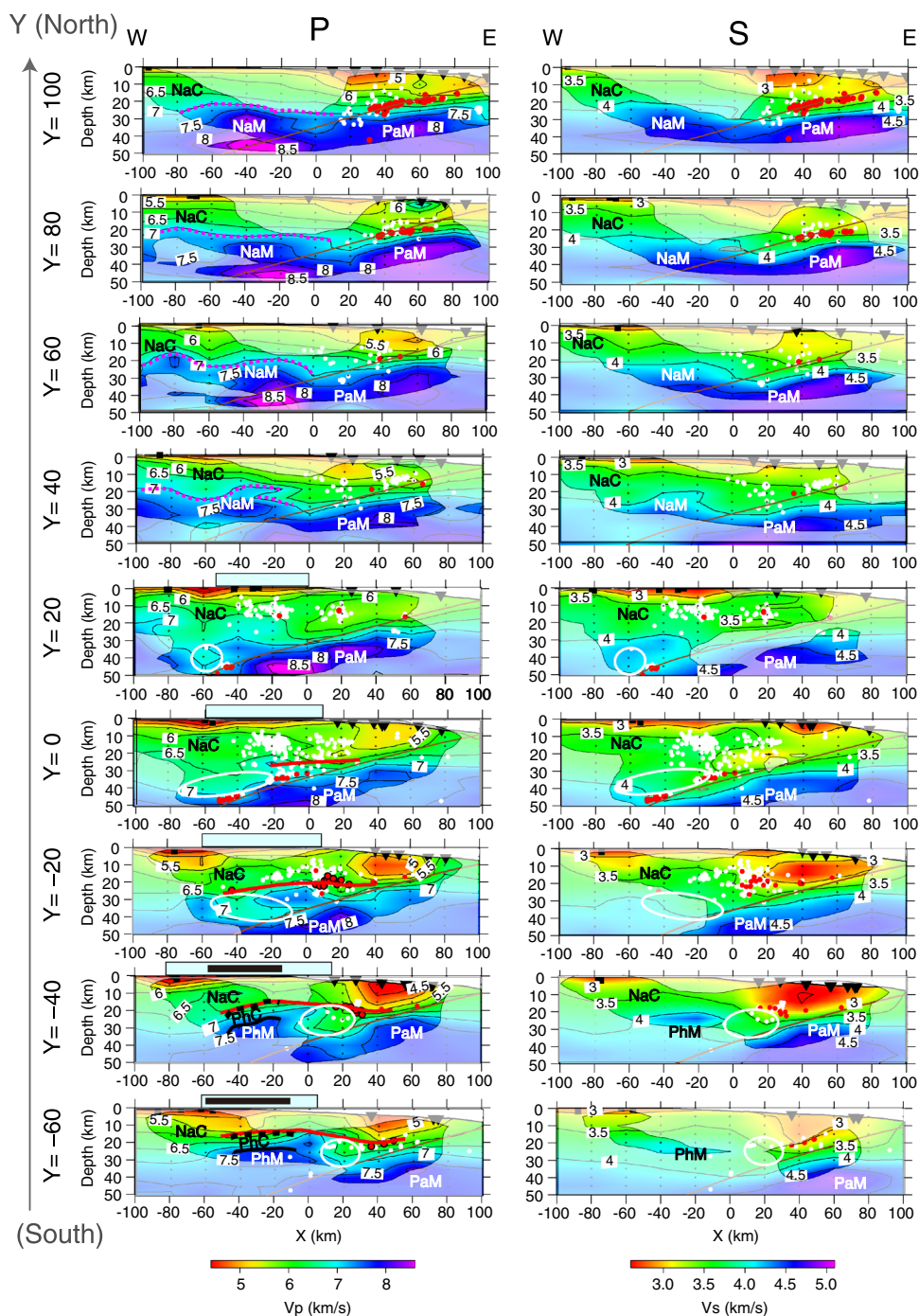


**Fig. 7** Results of the tomographic inversion along the X-axis. The black triangles and squares in each panel indicate the stations within 10 km of each section. The white and red dots indicate all faulting earthquakes and low-angle thrust-faulting earthquakes within 10 km of each section, respectively. The brown line indicates the depths of the upper boundaries of the PAC (Nakajima et al. 2009). PaM, NaC, NaM, PhC, and PhM indicate the crustal (C) and mantle (M) parts of the three plates: PAC (Pa), NA (Na), and PHS (Ph). The areas surrounded by white lines indicate low-velocity regions in the PHS. The magenta dashed lines on the sections north of  $Y = 40$  km indicate the smoothed iso-velocity contour of  $V_p = 7.0$  km/s in the NA. The black bold and dashed lines on the sections south of  $Y = -40$  km represent the iso-velocity contours of  $V_p = 7.5$  km/s in the PHS and the top of the crust of the PHS, respectively (see the text for details). The red circles with bold black outlines indicate the low-angle thrust-faulting earthquakes used to estimate the upper boundary of the PHS. The bold red lines indicate the newly proposed upper boundary of the PHS. The black and light blue lateral bars at the top of each cross-section indicate slow slip areas with slips larger than 5 cm in the 2007, 2011, and 2014 SSEs (Hirose et al. 2014; Sato et al. 2017) and larger 1 cm in the 2014 SSEs (Sato et al. 2017)

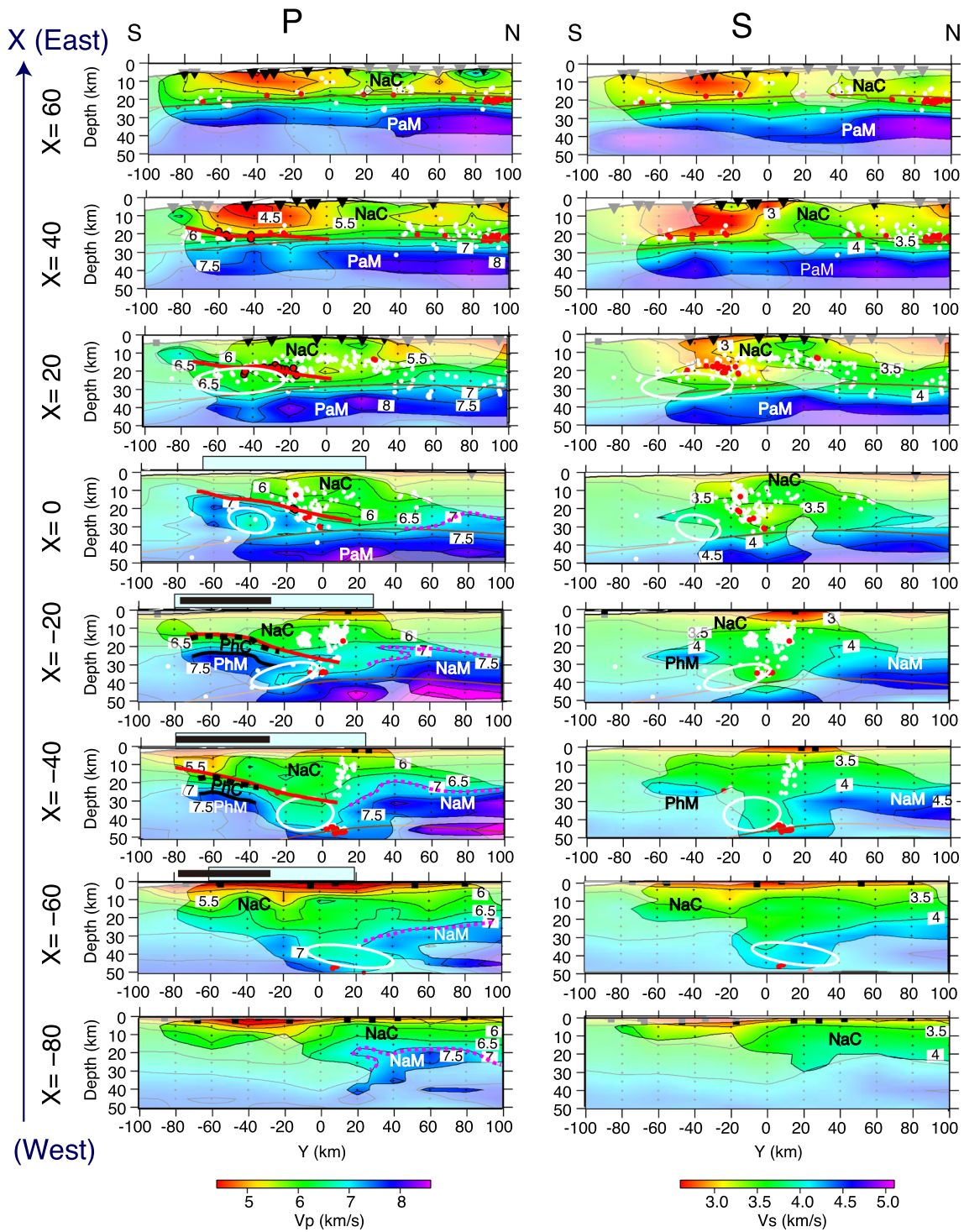


**Fig. 8** Results of the tomographic inversion along the Y-axis. The symbols are defined as in Fig. 7

3.3–4.0 km/s, respectively, surrounded by the white circles in Figs. 7 and 8, which will be discussed later. A notable low-velocity anomaly is located near the Japan Trench at depths shallower than 15 km ( $X=20\text{--}60$  km

south of  $Y=-20$  km in Fig. 7 and from  $Y=-60$  km to  $Y=-10$  km east of  $X=40$  km in Fig. 8), which Ito et al. (2017b) attributed to the existence of quartzite and fluid expelled from the PAC and PHS plates.

## RF images

Additional file 1: Figure S6 shows our time-domain RFs at each OBS, where large RF amplitudes are observed near the theoretical travel time of  $P_s$ -waves converted at the upper boundary of the PAC. Here, we calculated the travel time using a one-dimensional velocity model derived from the tomographic results in this study and the depth of the upper boundary of the PAC given in Nakajima et al. (2009). Several peaks are also observed at shorter lag times than the  $P_s$ -waves converted at the upper boundary of the PAC, which suggest the presence of interfaces in the overriding NA and PHS plates. We give a detailed explanation of the time-domain RF features in Additional file 1.

Figure 9a–c shows the depth profiles A–A', B–B', and C–C' of the depth-domain RFs, respectively, in the northern part of the studied area where the subducted PHS is not present. Each RF section is made by stacking RFs from OBSs within a 50-km-wide box on both sides of each profile in Fig. 4. The top of the vertical axis (0 km) corresponds to the sea surface.

The positive  $P_s$  phase can be traced at depths of 10–15 km and distances of 50–80 km in the A–A' profile (phase “1” in Fig. 9f). Below phase “1,” the positive RF phase “2” can be observed at distances of 60–75 km slightly above the upper boundary of the PAC (Nakajima et al. 2009). Based on their locations and depths, phases “1” and “2” are associated with interfaces in the NA crust. Along the upper boundary of the PAC, we observed several  $P_s$  phases with negative polarity, indicated as phase “3,” even though they are not clear. The polarities of the  $P_s$  phases from the upper boundary of the PAC are expected to be negative because the  $V_p$  value of the upper crust of the subducting PAC (5.0–6.0 km/s) is slower than those of the crust (5.5–7.0 km/s) and mantle (7.4–7.9 km/s) parts of the overriding NA (e.g., Miura et al. 2003; Ito et al. 2005). Phase “3” may therefore be converted waves from the upper boundary of the PAC. Beneath phase “3,” several  $P_s$  phases with positive polarity indicated as phase “4” are imaged. Phase “4” shifts westward with depth. In the B–B' profile (Fig. 9b), the same  $P_s$  phases as those in profile A–A' are observed. In the C–C' profile, phase “2” is clearly observed at distances of 25–50 km. Phase “2” appears to continue to the landward area. We interpret the above-described phases in “[Interfaces and velocity structures of NA and PAC](#)” section together with the velocity structure and the hypocenters of the low-angle thrust-faulting earthquakes.

Figure 9d and e shows the depth-domain RFs in the southern part of the studied area, where PHS is subducted (Uchida et al. 2009). We used the RF data of the OBSs north and south of approximately 35°N for the

depth-domain RF, which are projected on the D–D' (Fig. 9d) and E–E' (Fig. 9e) profiles, respectively. The horizontal axis is expressed using the X coordinates in Fig. 4. Note that the RF data in the southern region were compiled primarily from the SPOBS data, which have an ambiguity of 180° in the horizontal orientation. No continuous phase is observed in the E–E' profile due to the insufficiency and/or low quality of the data. Meanwhile, the most pronounced feature is that the horizontal  $P_s$  phases can be continuously traced at a depth of approximately 20 km immediately above the upper boundary of the PAC in the D–D' profile (phases “5” and “6” in Fig. 9i). Due to the 180° ambiguity in the horizontal orientation, we also made an RF image in Fig. 9j in which the RF amplitudes are shown by their absolute values. Horizontal  $P_s$  phases are also observed in Fig. 9j, as in Fig. 9d. We interpret phases “5” and “6” in “[Upper boundary and eastern limit of PHS](#)” section together with the velocity structure and newly proposed upper boundary of the PHS.

## Discussion

### Interfaces and velocity structures of NA and PAC

In Fig. 10, we compare the major  $P_s$  phases imaged in the RF analysis, the  $P$ -wave velocity structure, and the low-angle thrust-faulting earthquakes to interpret the interfaces and the velocity structure in the northern part of the studied area.

Phase “1” is located at  $V_p$  values of 5.5–6.0 km/s in the crustal part of the NA. From its location and polarity, we interpreted phase “1” to be the converted waves at the Conrad discontinuity (e.g., Miura et al. 2003; Ito et al. 2005). Phase “2” was imaged at  $V_p$  values of 6.0–7.0 km/s, which are close to the velocities at the bottom of the crust of the NA ( $V_p=7.0$  km/s) (e.g., Miura et al. 2003; Ito et al. 2005). We therefore attributed phase “2” to the converted waves at the Moho discontinuity in the NA. Because the Moho discontinuity was not necessarily observed over the entire studied region, we assumed the smoothed iso-velocity contour of  $V_p=7.0$  km/s to be the Moho discontinuity (the top of the mantle part in the NA). We indicate the smoothed iso-velocity contour of  $V_p=7.0$  km/s in the  $P$ -wave velocity sections north of  $Y=40$  km by the magenta dashed lines in Figs. 7 and 8.

We interpreted the negative  $P_s$  phase “3” to be converted waves from the upper boundary of the PAC based on its polarity and location. The location of phase “3,” the hypocenter distributions of the low-angle thrust-faulting earthquakes, and the previously reported geometry of the PAC (Nakajima et al. 2009) are all mutually consistent. Below the upper boundary of the PAC, phase “4” is located at  $V_p$  values of the 7.0–8.0 km/s, which is comparable to the top of the mantle of the PAC ( $V_p>7.5$  km/s)

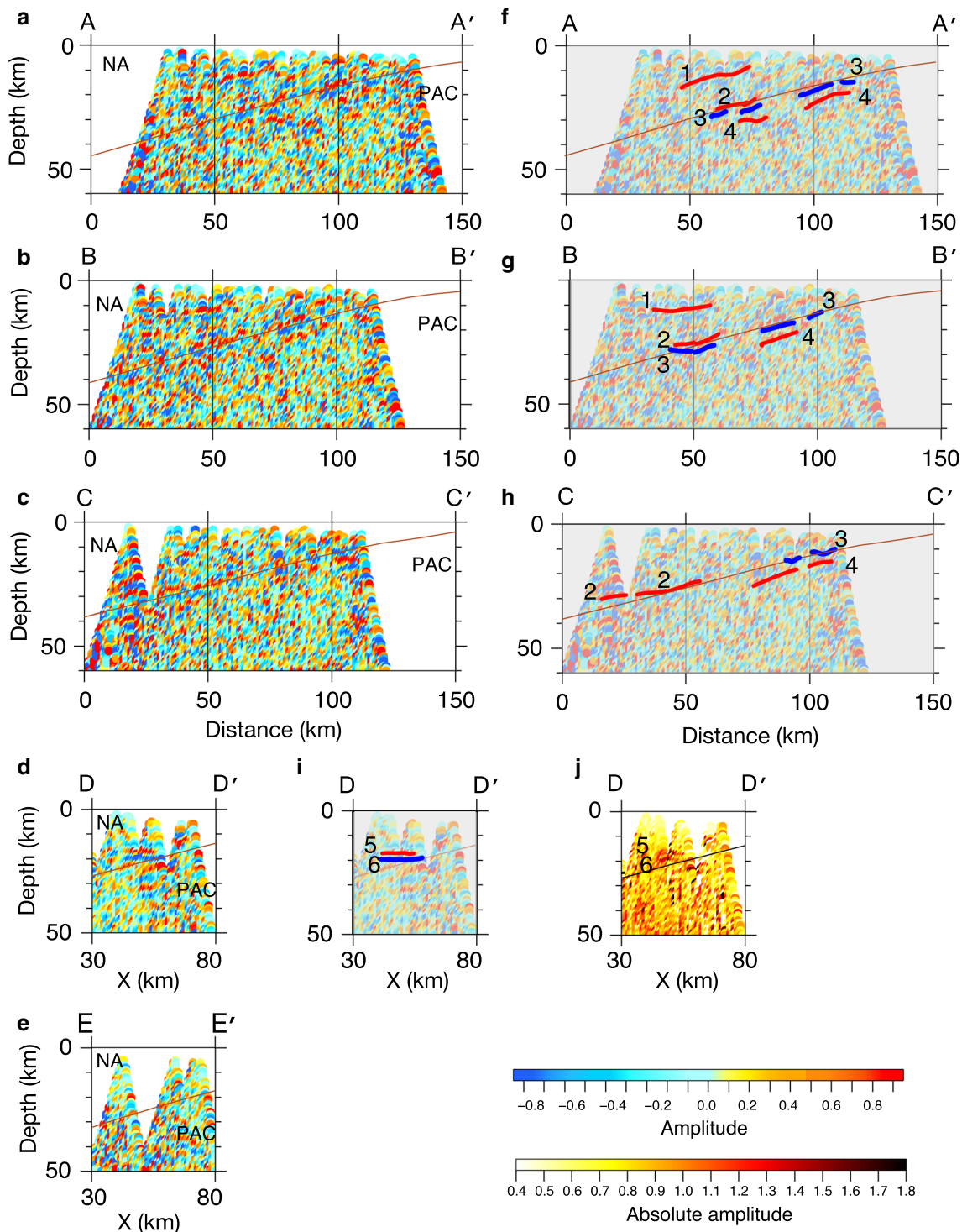
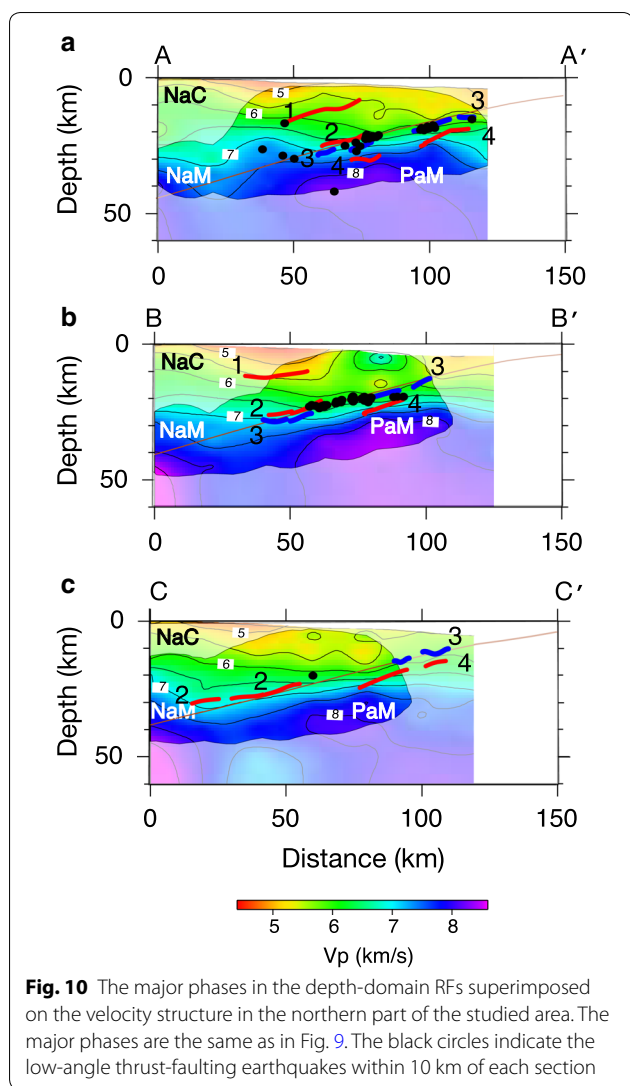


**Fig. 9** Depth-domain RFs. The locations of each section are defined as in Fig. 4. Red represents positive RF amplitudes, indicating a velocity increase downwards, while blue represents negative RF amplitudes, indicating a velocity decrease downward. The brown line indicates the depths of the upper boundaries of the PAC (Nakajima et al. 2009). The RF sections in **a–c** were made from OBSs that were in the area where the PHS is not present (Uchida et al. 2009), and the sections in panels **f–h** show the major emphatic phases. The RF sections in **d** and **e** were made from OBSs only north or south of 35°N, respectively, in the area where the PHS is subducted. The section in panel **i** shows the major emphatic phases in **d**. The RF section in **j** was made from the same OBSs as that in **d**, but its RF amplitudes are shown as absolute values. Interpretations of the interfaces are as follows: (1) Conrad in the NA, (2) Moho in the NA, (3) the plate boundary between the NA and the PAC, (4) the oceanic Moho in the PAC, (5) the bottom of the low-velocity anomaly in the NA, and (6) the plate boundary between the NA and the PHS



(Nakajima et al. 2009). We therefore attributed phase “4” to the converted waves at the Moho discontinuity in the PAC. Simultaneously, we consider  $V_p$  values of  $>7.5$  km/s to be appropriate for the mantle of the PAC in the studied region.

**Upper boundary and eastern limit of PHS**

We estimated the location of the upper boundary of the PHS based on the velocity structure, the hypocenters of the low-angle thrust-faulting earthquakes, and previous refraction studies.

We used the mantle part of the subducting slabs in the tomographic images, the RF image, the crustal thickness estimated by previous studies to define the upper boundary of the PHS because the tomographic results show that the mantle parts of the subducting slabs are imaged well and that the crustal parts of the subducting slabs are

not resolved well due to the limited resolution. In the northern part of the studied region, numerous low-angle thrust-faulting earthquakes were observed approximately 6–9 km above the mantle of the PAC ( $V_p > 7.5$  km/s) (Figs. 7 and 10). These earthquakes are located at the upper boundary of the PAC as inferred from the RF images; therefore, the crustal thickness of the PAC is thought to be 6–9 km. This is consistent with the PAC crustal thickness of 7–9 km obtained by previous refraction studies (e.g., Miura et al. 2003; Ito et al. 2005). We applied the above approach to define the upper boundary of the PHS, namely, we used the top of the mantle of the PHS to define the upper boundary of the PHS by referring to the crustal thicknesses obtained in previous studies. We assumed that the iso-velocity contour of  $V_p = 7.5$  km/s indicated the top of the mantle of the PHS (Matsubara et al. 2005; Nakajima et al. 2009). We indicate the iso-velocity contour of  $V_p = 7.5$  km/s in the *P*-wave velocity sections at  $Y = -40$  km and  $Y = -60$  km in Fig. 7 and at  $X = -20$  km and  $X = -40$  km in Fig. 8 by black lines.

We performed a restoring resolution test (RRT) (e.g., Zhao et al. 1992) to examine whether the mantle part of the PHS can be resolved by our dataset. In the test, we calculated synthetic arrival times using the velocity model and hypocenters obtained by this study as the input model, added random noise to the synthetic data with standard deviations of 0.1 s for the *P*-waves, and then obtained velocity models using the synthetic data. We compared the input velocity model and the RRT result in the N–S cross-sections in Additional file 1: Figure S7. The mantle parts of the PHS at  $X = -20$  km and  $X = -40$  km are restored as per the input model, indicating that the mantle part of the PHS, including the relatively low-velocity part ( $V_p$  values of 6.5–7.0 km/s in Additional file 1: Figure S7), are well resolved by our dataset.

We attributed the region “PhC”, immediately above the mantle of the PHS, to the crust of the PHS as shown in the *P*-wave velocity sections in Figs. 7 and 8. The top of the crust of the PHS is represented by a black dashed line at  $Y = -40$  km and  $Y = -60$  km in Fig. 7. The crustal thickness of the PHS is assumed to be approximately 10 km, as estimated by both a refraction study at the Izu–Bonin forearc region (Kamimura et al. 2002) and a land-based tomographic study beneath the Kanto region (Matsubara et al. 2005). The  $V_p$  values (6.5–7.5 km/s) of the assumed crust of the PHS in this study are nearly the same as those obtained by Matsubara et al. (2005), who estimated the  $V_p$  values of the subducted PHS crust to be 6.4–7.5 km/s at depths of 30–70 km.

The low-angle thrust-faulting earthquakes with orientations consistent with PHS subduction were also used

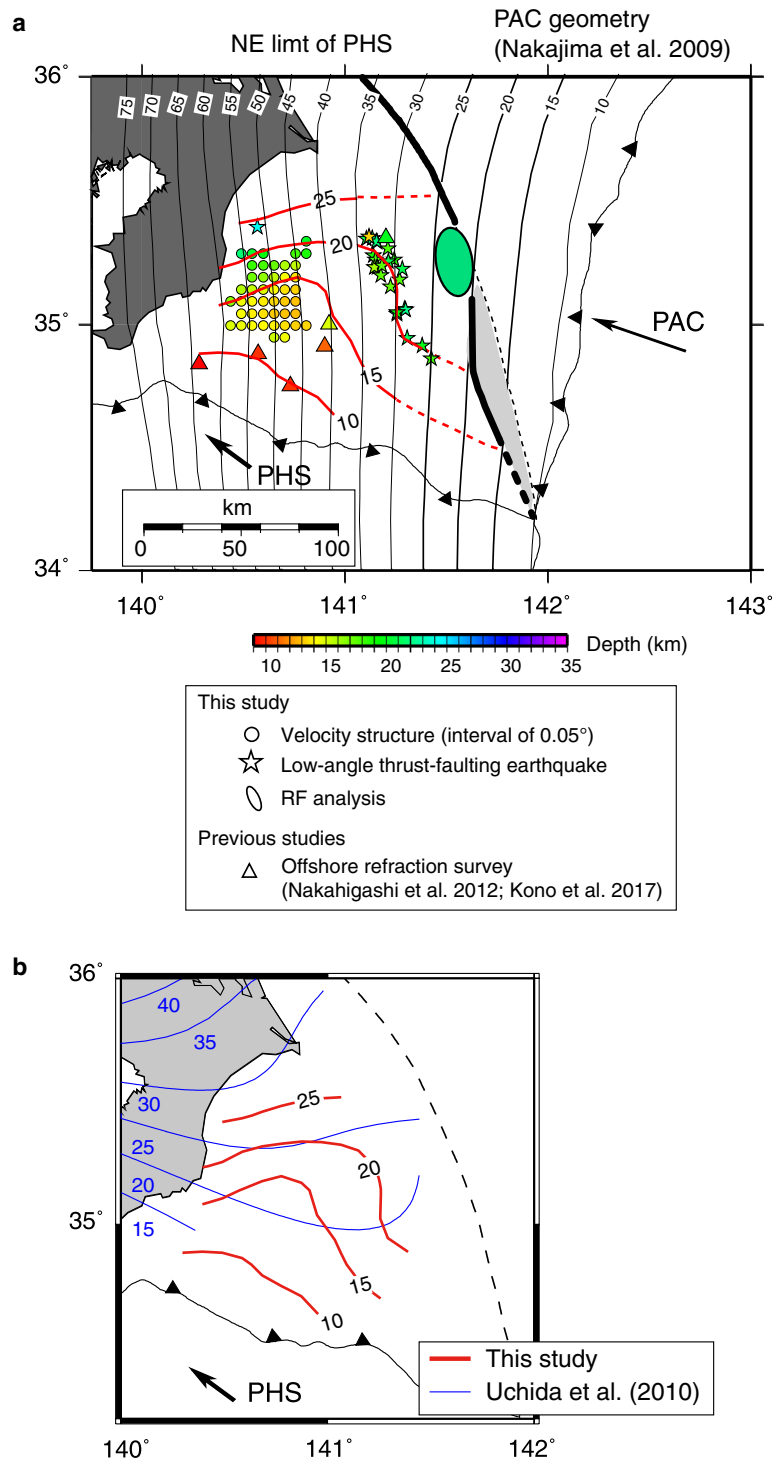


**Fig. 11** Geometries of the upper boundary of the PHS compared to previous study. **a** The red solid and broken lines show the iso-depth contours of the upper boundary of the PHS based on the tomographic images (circles), the locations of low-angle thrust-faulting earthquakes (stars), and previous refraction studies (triangles). The depths from previous refraction studies are 9 km, 10 km, and 11 km for the upper boundaries of the PHS along a survey line in Kono et al. (2017) and 10 km, 15 km, and 20 km along a survey line in Nakahigashi et al. (2012). The colors of the symbols correspond to the depth. The green region shows the area where phase “6” (the converted wave at the plate boundary between the NA and PHS) was observed in the RF analysis. The north–south trending curves indicate the iso-depth contours of the upper boundary of the PAC. The black bold and broken lines define the edge of the PHS, and the gray-shaded zone presents the gap between this study and that of Uchida et al. (2009). **b** The red and blue lines show the depths of the upper boundaries of the PHS derived in this study and those derived by Uchida et al. (2010), respectively

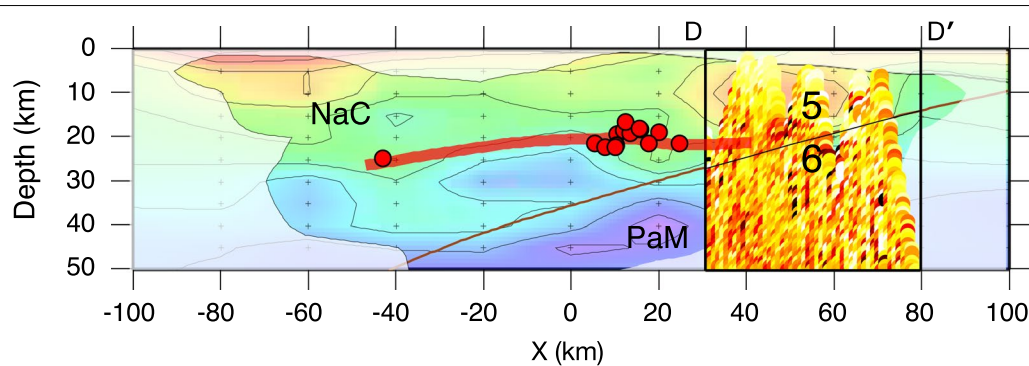


**Fig. 12** The depth-domain RFs in the D–D′ profile superimposed on the velocity structure at  $Y = -20$  km. The bold red line shows the newly proposed upper boundary of the PHS, which is projected on  $Y = -20$  km. The red circles with bold black outlines indicate the low-angle thrust-faulting earthquakes used to estimate the upper boundary of the PHS

to determine the PHS upper boundary when they were available. We show these earthquakes as red circles with bold outlines on the  $P$ -wave velocity sections in Figs. 7 and 8. Figure 6c also shows the focal mechanisms and locations of the earthquakes used to estimate the upper boundary of the PHS (the magenta focal mechanism in the figure).

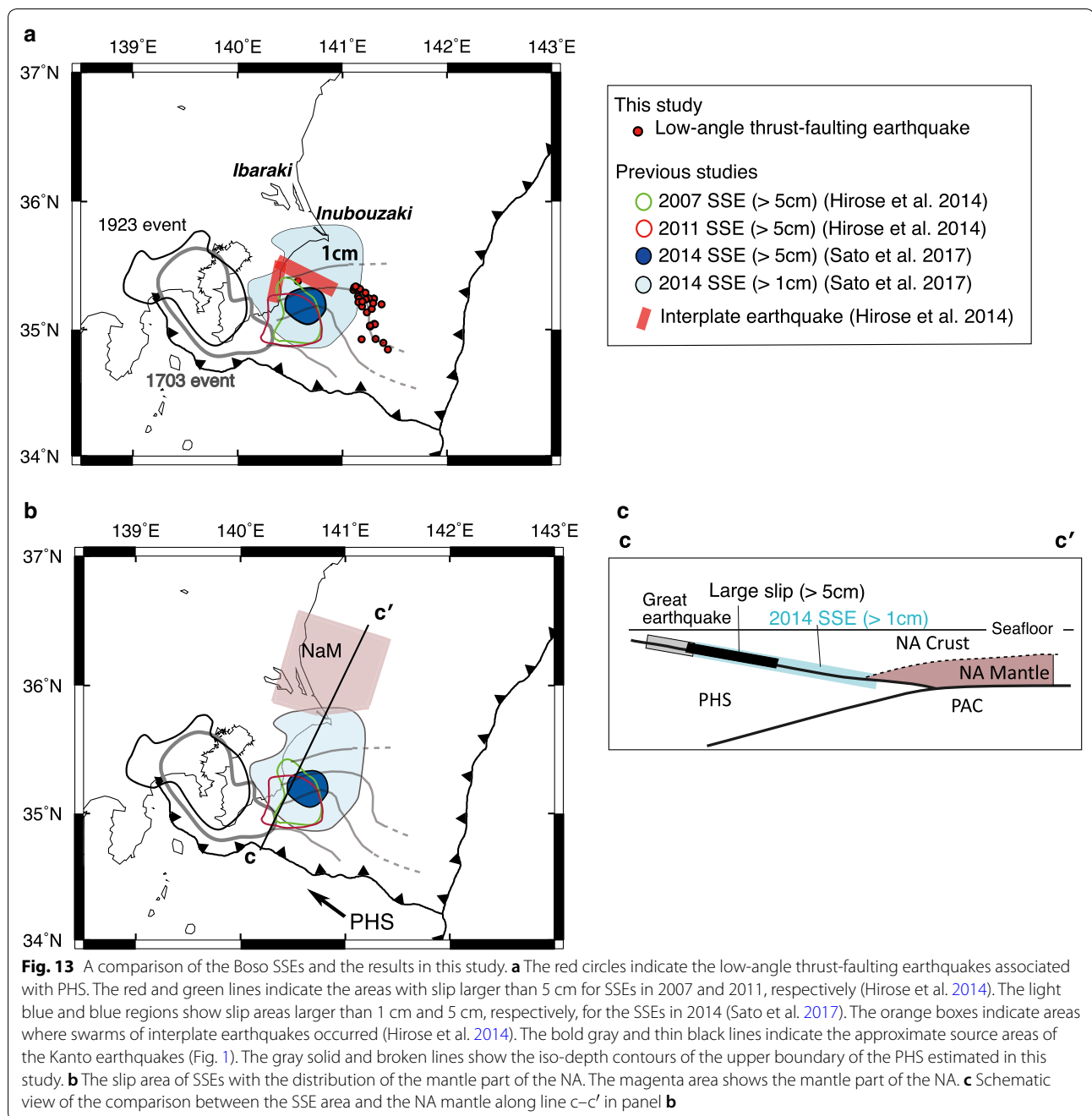
We propose iso-depth curves of the upper boundary of the PHS in Fig. 11a. We also plot the depths used to draw the iso-depth curves, which were estimated from the top of the crust of the PHS in the tomographic images (denoted by circles), the hypocenters of the low-angle thrust-faulting earthquakes (denoted by stars), and previous refraction surveys (denoted by triangles) (Kono et al. 2017; Nakahigashi et al. 2012). The colors of the symbols in Fig. 11a represent the depths of the upper boundary of the PHS. The upper boundary delineated by this study dips toward the northwest, which is nearly parallel to the convergent direction of the PHS. The upper boundary has a saddle-like geometry between  $140.5^\circ\text{E}$  and  $141.0^\circ\text{E}$ , where the boundary is distorted upward by a few kilometers. This may indicate buckling of the PHS due to its collision with the deeper PAC. The estimated depths of the upper boundary are shown by the red bold lines in Figs. 7 and 8.

The geometry of the upper boundary of the PHS under the Boso Peninsula has been extensively studied (e.g., Iidaka et al. 1990; Ishida 1992; Sekiguchi 2001; Sato et al. 2005; Hori 2006; Kimura et al. 2006; Wu et al. 2007; Hirose et al. 2008; Toda et al. 2008; Uchida et al. 2010). Of these previous studies, we compare our results to those of Uchida et al. (2010) in Fig. 11b, as this is the only study that estimated the upper boundary of the PHS not only in the land area but also in the offshore area by analyzing repeating earthquakes and seismic waves converted at the plate boundary. East of  $141.3^\circ\text{E}$ , our upper

boundary at a depth of 20 km is nearly consistent with that in Uchida et al. (2010). Conversely, west of  $141.3^\circ\text{E}$ , the upper boundaries of the PHS delineated by this study are shallower by approximately 5–6 km and 3 km than those delineated by Uchida et al. (2010) at depths of 15–20 km and 25 km, respectively. Because Uchida et al. (2010) used land-based observations that relied on earthquakes whose depths were not accurate in the offshore area, this discrepancy may arise from our improved hypocenter locations using OBS data.

In Fig. 12, we compare the depth-domain RFs in the D–D′ profile (Fig. 9j), the velocity structure ( $Y = -20$  km in Fig. 7), and the upper boundary proposed in Fig. 11a. The interface (phase “6”) is smoothly connected with the proposed upper boundary of the PHS, which indicates that phase “6” can be attributed to the converted waves at the upper boundary of the PHS. We plotted the area where phase “6” was observed in Fig. 11a. The upper boundary adjacent to the northeast edge of the PHS is delineated for the first time. As shown in Figs. 7 and 8 (and found by Ito et al. (2017b)), a low-velocity anomaly exists in the crust of the NA at depths of  $\leq 15$  km in the southern part of the studied region. The bottom of the low-velocity anomaly is located close to phase “5” at  $X = 20$ – $70$  km in Fig. 12. Phase “5” may therefore be attributable to the converted wave at the bottom of the low-velocity anomaly.

We investigated the geometry of the PHS slab further trenchward by extrapolating the proposed iso-depth curves (the bold red curves in Fig. 11a) trenchward. The constraint for the extrapolation was that the upper boundary of the PHS must be coincident with the upper boundary of the PAC denoted by the north–south trending iso-depth curves in Fig. 11a at the northeastern limit of the PHS. We manually extended the PHS iso-depth curves of 15 km, 20 km, and 25 km trenchward to



connect to the same depths of the upper boundary of the PAC, as shown by the red dotted curves. We therefore defined the edge of the PHS (the contact line with the PAC upper boundary), as denoted by the black bold and dotted curve, by connecting the edge at a depth of 15 km and the triple junction. Uchida et al. (2009) proposed the northeastern limit of the PHS based on the slip directions of interplate earthquakes west of 141.5°E. However, the geometry and the presence of the PHS slab to the east of

141.5°E have not been well constrained due to the lack of slip direction data, and the northeastern limit had been estimated by connecting the limit location of the PHS at 141.5°E and the triple junction (the thin dotted curve in Fig. 11a). The edge defined by this study suggests that the PHS is not present in the gray-shaded zone (the gap between the northeastern limits in the study of Uchida et al. (2009) and those in this study). In other words, the gray-shaded zone is a part of the NA crust.

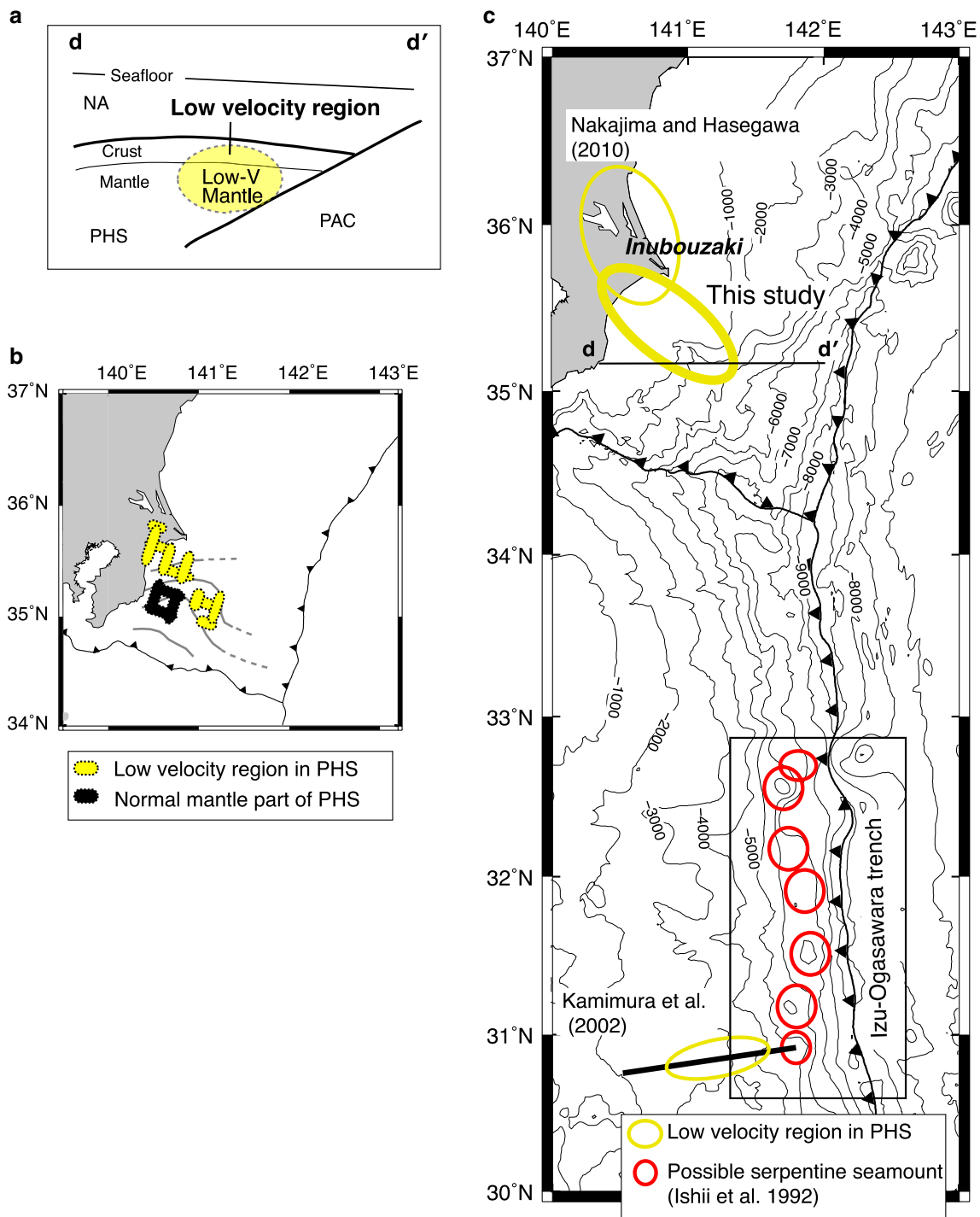


**Fig. 14** Low-velocity region in the PHS. **a** Schematic view for the interpretation of the low-velocity region along line d–d' in **c**. **b** Distribution of the low-velocity region in this study. Areas shaded yellow and black show the locations of the low-velocity region in the PHS and the normal mantle of the PHS, respectively. **c** Distribution of the low-velocity region and serpentine seamounts. Yellow and red circles indicate the locations of the low-velocity anomaly according to this and previous studies (Kamimura et al. 2002; Nakajima and Hasegawa 2010) and possible serpentine seamounts (Ishii et al. 1992), respectively. The square shows the study area of Ishii et al. (1992)

The geometry of the eastern edge of the subducted PHS near the Sagami Trough may be related to the change in the subduction direction of the PHS. Our study suggests that the eastern edge of the PHS has a north–west–southeast trend between the triple junction and 141.6°E, which changes to a north–south trend north of 34.7°N. The inflection point of the slab edge at 141.6°E and 34.7°N is located approximately 65 km north of the Sagami Trough. Considering the north component of the present relative speed of the PHS and NA (3.0–3.8 cm/a) (e.g., Seno and Maruyama 1984; DeMets et al. 2010), this inflection point corresponds to the PHS that was subducted at 3.0–2.4 Ma. This is close to the time when the subduction direction changed from northward to north–eastward at 1–3 Ma, which has been suggested by previous geological studies (e.g., Yamaji 2000; Kamata 2003; Takahashi 2006). The change in the subduction direction might result in the inflection of the eastern edge of the subducted PHS slab even though other possibilities, such as the deformation of the thin part of the PHS near the edge due to the interaction with the PAC, may also explain this inflection.

#### Comparison of the structure to SSEs off Boso

We show the areas of the SSEs that occurred in 2007, 2011, and 2014 (Hirose et al. 2014; Sato et al. 2017) in Fig. 13a, b. The area of the 2014 SSEs was reliably determined using data from both GNSS and ocean-bottom pressure gauges immediately above the SSEs (Sato et al. 2017), which could constrain the eastern limit of the slip area well. The slip areas larger than 5 cm in 2007, 2011, and 2014 SSEs overlap significantly, and the slip area larger than 1 cm in the 2014 SSEs extends to the offshore area at approximately 141.2°E.

We compared the slip areas of the SSEs with that of the interplate earthquakes found by this study in Fig. 13a. The areas of the SSEs, the regular low-angle thrust-faulting earthquakes, and the great Kanto earthquakes are complementarily distributed in the off-Boso area. Most of the low-angle thrust-faulting earthquakes occurred at 141–141.5°E, which is outside the 2014 SSE area. To the north and west of the SSEs with slips greater than 5 cm, swarms of interplate earthquakes (the orange boxes in Fig. 13a) took place during the 2007 and 2011 SSEs (Hirose et al. 2014). The great Kanto earthquakes occurred south of the SSE areas, suggesting a strong coupling at the plate boundary between the PHS and the NA. When the above observations are combined, the SSE areas with slips greater than 5 cm do not overlap the areas of the seismogenic zone of the great Kanto earthquakes and the regular interplate earthquakes. A spatial separation of the slow slip area and the regular earthquakes was also reported for the Hikurangi subduction zone in New

Zealand (Bartlow et al. 2014) and the Ryukyu Trench (Yamamoto et al. 2018), likely indicating spatial differences in the fault friction properties on plate boundaries.

To examine the relationship between the structure of the overriding plate and the SSE area, we indicate the slip area larger than 1 cm in the 2014 SSEs (light blue) and the slip areas larger than 5 cm in the 2007, 2011, and 2014 SSEs (black) by lateral bars in Figs. 7 and 8. In addition, we plot the mantle part of the NA ( $V_p > 7.0$  km/s) in Fig. 13b. It is clear that the large-slip areas of the SSEs in 2007, 2011, and 2014 are exclusively located at the plate boundary of the contact zone between the NA and PHS crusts. The northern edge of the slip area of the 2014 SSEs is coincident with the intersection of the Moho discontinuity in the NA and the subducting PHS (Fig. 13c). The slip area larger than 1 cm in the 2014 SSEs extends to the region beneath Inubouzaki on the Boso Peninsula. This slip distribution is likely robust because the GNSS data observed at Inubouzaki show significant displacement during the 2014 SSEs (Ozawa 2014; Sato et al. 2017). Significant displacement beneath Inubouzaki was also observed during the 2007 SSEs (Ozawa et al. 2007), and the slip area of the 2007 SSEs might extend to the region beneath Inubouzaki, even though the slip was less than 5 cm there.

The localization of SSEs at the crust–crust contact zone in the dip direction was also observed in the Tokai region (e.g., Kodaira et al. 2004; Matsubara et al. 2009; Kato et al. 2010). Kato et al. (2010) obtained the velocity structure and the location of the Moho discontinuity by a tomographic inversion and an RF study in the Tokai region, 300 km west of the off-Boso area. The SSE area was limited to the crust–crust contact zone, and deep low-frequency earthquakes only occurred beneath the mantle wedge of the overriding plate, which is consistent with the SSE localization off Boso. They proposed that the variation in the fluid pressure depends on the heterogeneous fluid transport properties in the hanging wall of the plate boundary, which controls the slip properties along the plate boundary.

#### Low-velocity zone in PHS

The region with  $V_p = 6.5$ – $7.0$  km/s and  $V_s = 3.3$ – $4.0$  km/s, surrounded by white circles in Figs. 7 and 8, is located immediately below the upper boundary of the PHS (the red lines in the figures) and has a thickness of 10–20 km. These velocities are lower than those in the PHS mantle (with  $V_p$  and  $V_s$  values of 7.5–8.0 km/s and 4.0 km/s, respectively). We believe that this low-velocity region consists of the normal crust and the low-velocity mantle of the PHS, as shown in Fig. 14a. Figure 14b shows the horizontal distribution of the low-velocity

region and the normal mantle part of the PHS (“PhM” in Figs. 7 and 8).

In the RRT (Additional file 1: Figure S7), we showed that the low-velocity zone in the PHS can be resolved by our dataset. We performed another RRT to examine whether the low-velocity mantle of the PHS could be an artifact due to the limited resolution. In the test, we replaced the low-velocity mantle with a velocity of 7.5 km/s in the input model, which is the velocity in the normal mantle outside the low-velocity zone, and then calculated the synthetic data. We compare the input velocity model to the result of the RRT in Additional file 1: Figure S8. The restored model obtained by the synthetic data is 7.5 km/s or higher in the mantle part of the PHS, which is consistent with the velocities in the input model. This RRT indicates that the low-velocity mantle of the PHS is not an artifact due to, for example, limited ray coverage, but is instead a robust feature from our current dataset.

Several land-based studies have reported a low-velocity anomaly in the PHS beneath Inubouzaki on the Boso Peninsula (enclosed in yellow circles in Fig. 14c) (Uchida et al. 2009; Nakajima et al. 2009; Nakajima and Hasegawa 2010). The  $V_p$  and  $V_s$  values of the low-velocity anomaly are <6.8 km/s and <3.8 km/s, respectively, which are consistent with the values obtained in this study. The low-velocity region found in this study partially overlaps beneath the coastline with the previously reported low-velocity anomaly and extends to the offshore area, an area that previous studies did not resolve primarily due to a lack of data in the oceanic area.

Uchida et al. (2009) and Nakajima and Hasegawa (2010) suggested that serpentinized peridotite, which formed in the PHS at the Izu–Bonin forearc region prior to subduction, is responsible for the low-velocity anomaly. Uchida et al. (2009) also suggested that serpentinized peridotite is responsible for the weak coupling between the PHS and the PAC because the low-velocity anomalies are distributed in the weak interplate-coupling zone between the two plates. Kamimura et al. (2002) conducted a refraction survey in the Izu–Bonin forearc region (Fig. 14c) and found a low-velocity anomaly with  $V_p$  values of 6.4–6.8 km/s in the mantle of the PHS 40–130 km from the Izu–Ogasawara trench. Considering that serpentine seamounts were observed in the forearc region (Ishii et al. 1992), Kamimura et al. (2002) attributed the low-velocity anomaly to the presence of serpentinized peridotite.

We attribute the low-velocity region detected in this study to serpentinized peridotite, as proposed by Kamimura et al. (2002), Uchida et al. (2009), and Nakajima and Hasegawa (2010), due to the velocity values and the location of the low-velocity region shown in Fig. 14c. The serpentinized peridotite zone remains after

the subduction of the PHS and is likely distributed over a wide area along the subducted PHS.

## Conclusions

We performed a tomographic inversion using seismic data of local earthquakes from OBSs in the off-Boso area and land-based stations around the Boso Peninsula. We also applied an RF analysis to teleseismic  $P$  waveforms observed at the OBSs. We imaged the mantle parts of the PAC, NA, and PHS in the resulting velocity structure and identified numerous low-angle thrust-faulting earthquakes associated with PAC and PHS subduction. The upper boundary of the PHS near 141.5°E was imaged as seismic velocity discontinuities using the RF analysis. We summarize the conclusions derived from these investigations as follows.

- (a) We estimated the depths of the upper boundary of the PHS and PAC from the tomographic image, the locations of the low-angle thrust-faulting earthquakes, and the RF images. The upper boundary of the PHS is distorted upward by a few kilometers between 140.5 and 141.0°E. It is 3–6 km shallower than the upper boundary estimated by Uchida et al. (2010) west of 141.3°E. The delineated upper boundary of the PAC is nearly the same as that proposed by Nakajima et al. (2009).
- (b) We determined the eastern edge of the PHS based on the delineated upper boundary and the results of the RF analysis. The eastern edge of the PHS has a northwest–southeast trend between the triple junction and 141.6°E, which changes to a north–south trend north of 34.7°N. The change in the subduction direction at 1–3 Ma or the deformation of the edge might have resulted in the inflection of the eastern edge of the subducted PHS.
- (c) We compared the subduction zone structure, hypocenter locations, and past SSEs. Most of the low-angle thrust-faulting earthquakes identified in this study occurred outside the slow slip area, which indicates that the large-slip areas of the Boso SSEs and the regular low-angle thrust earthquakes along the upper boundary of the PHS are spatially separated. In addition, the slip areas of the SSEs are located exclusively at the plate boundary of the contact zone between the crustal parts of the NA and the subducting PHS. The localization of the SSEs at the crust–crust contact zone is delineated for the first time in the off-Boso area.
- (d) A relatively low-velocity region was detected in the PHS. We suggest that this low-velocity region can be attributed to the normal crust and low-velocity mantle of the PHS. The low-velocity mantle of the

PHS can be interpreted as serpentinized peridotite, which is also found in the PHS prior to subduction. The serpentinized peridotite zone remains after the subduction of the slab and is likely distributed over a wide area along the subducted PHS.

## Supplementary information

**Supplementary information** accompanies this paper at <https://doi.org/10.1186/s40623-019-1090-y>.

**Additional file 1. Figure S1:** Locations of stations. **Table S1:** Summary of JAMSTEC OBSs (BBOBSs and SPOBSs). **Table S2:** Summary of ERI OBSs (LTOBSs). **Figure S2:** Histogram of the magnitudes for local earthquakes. **Figure S3:** Example of seismic record for a local earthquake. **Figure S4:** Ray paths of seismic phases isolated from teleseismic P wave for seafloor observation. **Figure S5:** Hypocenters determined by tomoDD. **Additional Note 1:** Time-domain RFs. **Figure S6:** Examples of time-domain RFs. **Figure S7:** Results of the first RRT. **Figure S8:** Results of the second RRT.

## Abbreviations

PAC: Pacific Plate; NA: North American Plate; PHS: Philippine Sea Plate; OBS: ocean-bottom seismometer; BBOBS: broadband OBS; SPOBS: short-period OBS; LTOBS: long-term OBS; RF: receiver function; DWS: derivative weight sum.

## Acknowledgements

This study is partly supported by the Special Coordination Funds for the Promotion of Science and Technology (MEXT, Japan) designated as integrated research for the 2011 Tohoku Earthquake off the Pacific coast. We used data obtained from the Hi-net and F-net systems operated by NIED, and earthquake catalog published by JMA. We are grateful to Masaki Takahashi and Hikaru Iwamori for their advice regarding the geology and geodynamics around the off-Boso area. We also would like to thank Shinji Toda for providing us with advice about tectonics under the Kanto region. Our discussions with Hitoshi Hirose and Toshinori Sato regarding the Boso SSE were greatly appreciated. We also appreciate the help of Masaru Nakano in the analysis of the hypocenter locations and tomographic inversion. The editor Junichi Nakajima and two anonymous reviewers greatly helped to improve the manuscript.

## Authors' contributions

AI performed the observations of BBOBSs, the data processing, the analysis, and wrote the manuscript. TT supported the RF analysis and approved the manuscript. NU supported the interpretation and the discussion of the PHS subduction process, and approved the manuscript. YY supported the tomographic inversion and approved the manuscript. DS and RH approved the manuscript. HS performed the BBOBS observations and approved the manuscript. KO performed the SPOBS observations. KN and MS supported the data collection of OBSs by ERI. All authors read and approved the final manuscript.

## Funding

This study is partly supported by the Special Coordination Funds for the Promotion of Science and Technology (MEXT, Japan) designated as integrated research for the 2011 Tohoku Earthquake off the Pacific coast.

## Availability of data and materials

The datasets analyzed in the current study available from the corresponding author on reasonable request.

## Ethics approval and consent to participate

Not applicable.

## Consent for publication

Not applicable.

## Competing interests

The authors declare that they have no competing interests.

## Author details

<sup>1</sup> Research Institute for Marine Geodynamics, Japan Agency of Marine- Earth Science and Technology, 2-15 Natsushima-cho, Yokosuka, Kanagawa 237-0061, Japan. <sup>2</sup> Research Center for Prediction of Earthquakes and Volcanic Eruptions, Graduate School of Science, Tohoku University, 6-6, Aza-Aoba, Aramaki, Aoba-ku, Sendai, Miyagi 980-8578, Japan. <sup>3</sup> Department of Planetology, Graduate School of Science, Kobe University, 1-1 Rokkodai-cho, Nada-ku, Kobe, Hyogo 657-8501, Japan. <sup>4</sup> Department of Marine Resources and Energy, Tokyo University of Marine Science and Technology, 4-5-7, Konan, Minato-ku, Tokyo 108-8477, Japan. <sup>5</sup> Center for Geophysical Observation and Instrumentation, Earthquake Research Institute, University of Tokyo, 1-1-1, Yayoi, Bunkyo-ku, Tokyo 113-0032, Japan.

Received: 1 April 2019 Accepted: 16 October 2019

Published online: 25 October 2019

## References

- Ando M (1971) A fault-origin model of the great Kanto earthquake of 1923 as deduced from geodetic data. *Bull Earthq Res Inst Univ Tokyo* 49:19–32
- Bartlow NM, Wallace LM, Beavan RJ, Bannister S, Segall P (2014) Time-dependent modeling of slow slip events and associated seismicity and tremor at the Hikurangi subduction zone, New Zealand. *J Geophys Res* 119:734–753. <https://doi.org/10.1002/2013JB010609>
- Brocher TM (2005) Empirical relations between elastic wavespeeds and density in the earth's crust. *Bull Seismol Soc Am* 95(6):2081–2092. <https://doi.org/10.1785/0120050077>
- DeMets C, Gordon RG, Argus DF (2010) Geologically current plate motions. *Geophys J Inter*. <https://doi.org/10.1111/j.1365-246X.2009.04491.x>
- Frohlich C (1992) Triangle diagrams: ternary graphs to display similarity and diversity of earthquake focal mechanisms. *Phys Earth Planet Inter* 75:93–198
- Hirose F, Nakajima J, Hasegawa A (2008) Three-dimensional velocity structure and configuration of the Philippine Sea Slab beneath Kanto district, central Japan, estimated by double-difference tomography. *J Seismol Soc Jpn* 60:123–138 (in Japanese)
- Hirose H, Kimura H, Enescu B, Aoi S (2012) Recurrent slow slip event likely hastened by the 2011 Tohoku earthquake. *Earth Atmospheric Planet Sci*. <https://doi.org/10.1073/pnas.1202709109>:15157–15161
- Hirose H, Matsuzawa T, Kimura T, Kimura H (2014) The Boso slow slip events in 2007 and 2011 as a driving process for the accompanying earthquake swarm. *Geophys Res Lett* 41:2778–2785. <https://doi.org/10.1002/2014GL059791>
- Hori S (2006) Seismic activity associated with the subducting motion of the Philippine Sea plate beneath the Kanto district, Japan. *Tectonophysics* 417:85–100. <https://doi.org/10.1016/j.tecto.2005.08.027>
- Iidaka T, Mizoue M, Nakamura I, Tsukuda T, Sakai K, Kobayashi M, Haneda T, Hashimoto S (1990) The upper boundary of the Philippine sea plate beneath the western Kanto region estimated from S-P-converted wave. *Tectonophysics* 179:321–326. [https://doi.org/10.1016/0040-1951\(90\)90297-L](https://doi.org/10.1016/0040-1951(90)90297-L)
- Ishida M (1992) Geometry and relative motion of the Philippine Sea plate and Pacific plate beneath the Kanto-Tokai district, Japan. *J Geophys Res* 97:489–513
- Ishii T, Robinson PT, Maekawa H, Fiske R (1992) Petrological studies of peridotites from diapiric serpentinite seamounts in the Izu-Ogasawara-Mariana forearc, Leg 125. *Proc ODP Sci Results* 125:445–485
- Ishizuka O, Tani K, Reagan KM, Kanayama K, Umino S, Harigane Y, Sakamoto I, Miyajima Y, Yuasa M, Dunkley JD (2011) The timescales of subduction initiation and subsequent evolution of an oceanic island arc. *Earth Planet Sci Lett* 306:229–240. <https://doi.org/10.1016/j.epsl.2011.04.006>
- Ito A, Fujie G, Miura S, Kodaira S, Kaneda Y, Hino R (2005) Bending of the subducting oceanic plate and its implication for rupture propagation of large interplate earthquakes off Miyagi, Japan, in the Japan Trench subduction zone. *Geophys Res Lett* 32:L05310. <https://doi.org/10.1029/2004GL022307>
- Ito A, Sugioka H, Obana K, Hino R, Suetsugu D, Nakahigashi K, Shinohara M, Nakano M, Yamamoto Y (2017a) Upper boundaries of the Pacific and Philippine Sea plates near the triple junction off the Boso Peninsula deduced

- from ocean-bottom seismic observations. *Earth Planets Space*. <https://doi.org/10.1186/s40623-017-0608-4>
- Ito A, Yamamoto Y, Hino R, Suetsugu D, Sugioka H, Nakano M, Nakahigashi K, Shinohara M (2017b) Tomographic image of crust and upper mantle off the Boso Peninsula using data from an ocean bottom seismograph array. *Earth Planets Space*. <https://doi.org/10.1186/s40623-017-0703-6>
- Kamata H (2003) Subduction of the Philippine Sea Plate as bedrock and its tectonic significance on the formation of the Southwest-Japan Island Arc. *J Soc Mat Sci Japan* 52:444–451
- Kamimura A, Kasahara J, Shinohara M, Hino R, Shiobara H, Fujie G, Kanazawa T (2002) Crustal structure study at the Izu–Bonin subduction zone around 31°N: implications of serpentinized materials along the subduction plate boundary. *Physics Earth Plane Int* 132:105–129
- Kato A, Iidaka T, Ikuta R, Yoshida Y, Katsumata K, Iwasaki T, Sakai S, Thurber C, Tsumura N, Yamaoka K, Watanabe T, Kunitomo T, Yamazaki F, Okubo M, Suzuki S, Naoshi Hirata N (2010) Variations of fluid pressure within the subducting oceanic crust and slow earthquakes. *Geophys Res Lett* 37:L14310. <https://doi.org/10.1029/2010GL043723>
- Kennett BLN (1983) *Seismic wave propagation in stratified media*. Cambridge University Press, Cambridge
- Kennett BLN (2001) *The seismic wavefield. Volume I: Introduction and theoretical development*. Cambridge University Press, Cambridge
- Kimura H, Kasahara K, Igarashi T, Hirata N (2006) Repeating earthquake activities associated with the Philippine Sea plate subduction in the Kanto district, central Japan: a new plate configuration revealed by interplate aseismic slips. *Tectonophysics* 417:101–118. <https://doi.org/10.1016/j.tecto.2005.06.013>
- Kodaira S, Iidaka T, Kato A, Park JO, Iwassaki T, Kaneda Y (2004) High pore fluid pressure may cause silent slip in the Nankai Trough. *Science* 304:1295–1298. <https://doi.org/10.1126/science.1096535>
- Kono A, Sato T, Shinohara M, Mochizuki K, Yamada T, Uehira K, Shinbo T, Machida Y, Hino R, Azuma R (2017) Geometry and spatial variations of seismic reflection intensity of the upper surface of the Philippine Sea plate off the Boso Peninsula, Japan. *Tectonophysics* 709:44–54. <https://doi.org/10.1016/j.tecto.2017.05.001>
- Langston CA (1977) The effect of planar dipping structure on source and receiver response for constant ray parameter. *Bull Seismol Soc Am* 67(4):1029–1050
- Langston CA (1979) Structure under Mount Rainier, Washington, inferred from teleseismic body waves. *J Geophys Res* 84:4749–4762
- Lomax A, Virieux J, Volant P, Berge C (2000) Probabilistic earthquake location in 3D and layered models: introduction of a Metropolis-Gibbs method and comparison with linear locations. In: Thurber CH, Rabinowitz N (eds) *Advances in Seismic Event Location*. Kluwer, Amsterdam, pp 101–134
- Matsu'ura M, Iwasaki T, Suzuki Y, Sato R (1980) Static and dynamical study on faulting mechanism of the 1923 Kanto earthquake. *J Phys Earth* 28:119–143
- Matsu'ura M, Noda A, Fukahata Y (2007) Geodetic data inversion based on Bayesian formulation with direct and indirect prior information. *Geophys J Int* 171(3):1342–1351
- Matsubara M, Hayashi H, Obara K, Kasahara K (2005) Low-velocity oceanic crust at the top of the Philippine Sea and Pacific plates beneath the Kanto region, central Japan, imaged by seismic tomography. *J Geophys Res* 110:B12304. <https://doi.org/10.1029/2005JB003673>
- Matsubara M, Obara K, Kasahara K (2009) High-VP/VS zone accompanying non-volcanic tremors and slow-slip events beneath southwestern Japan. *Tectonophysics* 472:6–17
- Matsuda T, Ota Y, Ando M, Yonekura N (1978) Fault mechanism and recurrence time of major earthquakes in southern Kanto district, Japan, as deduced from coastal terrace data. *Geol Soc Am Bull* 89:1610–1618
- Miura S, Kodaira S, Nakanishi A, Tsuru T, Takahashi N, Hirata N, Kaneda Y (2003) Structural characteristics controlling the seismicity of southern Japan Trench fore-arc region, revealed by ocean bottom seismographic data. *Tectonophysics* 363:79–102. [https://doi.org/10.1016/S0040-1951\(02\)00655-8](https://doi.org/10.1016/S0040-1951(02)00655-8)
- Müller RD, Sdrolias M, Gaina C, Roest WR (2008) Age, spreading rates and spreading symmetry of the world's ocean crust. *Geochem Geophys Geosyst* 9:Q04006. <https://doi.org/10.1029/2007GC001743>
- Nakahigashi K, Shinohara M, Mochizuki K, Yamada T, Hino R, Sato T, Uehira K, Ito Y, Murai Y, Kanazawa T (2012) P-wave velocity structure in the southernmost source region of the 2011 Tohoku earthquakes, off the Boso Peninsula deduced by an ocean bottom seismographic survey. *Earth Planets Space* 64:1149–1156. <https://doi.org/10.5047/eps.2012.06.006>
- Nakajima J, Hasegawa A (2010) Cause of M~7 intraslab earthquakes beneath the Tokyo metropolitan area, Japan: possible evidence for a vertical tear at the easternmost portion of the Philippine Sea slab. *J Geophys Res* 115:B04301. <https://doi.org/10.1029/2009JB006863>
- Nakajima J, Hirose F, Hasegawa A (2009) Seismotectonics beneath the Tokyo metropolitan area, Japan: effect of slab–slab contact and overlap on seismicity. *J Geophys Res* 114:B08309. <https://doi.org/10.1029/2008JB006101>
- Nakano M, Tonegawa T, Kaneda Y (2012) Orientations of DONET seismometers estimated from seismic waveforms. *JAMSTEC Rep Res Dev* 15:77–89
- Namegaya Y, Satake K, Shishikura M (2011) Fault models of the 1703 Genroku and 1923 Taisho Kanto earthquakes inferred from coastal movements in the southern Kanto area. *Ann Rep Act Fault Paleoeathquake Res* 11:107–120 (in Japanese with English abstract)
- Okada Y, Kasahara K, Hori S, Obara K, Sekiguchi S, Fujiwara H, Yamamoto A (2004) Recent progress of seismic observation networks in Japan—Hi-net, F-net, K-NET and KiK-net. *Earth Planets Space* 56:xx
- Ozawa S (2014) Shortening of recurrence interval of Boso slow slip events in Japan. *Geophys Res Lett*. <https://doi.org/10.1002/2014GL060072>
- Ozawa S, Suito H, Tobita M (2007) Occurrence of quasi-periodic slow-slip off the east coast of the Boso Peninsula, Central Japan. *Earth Planets Space* 59:1241–1245
- Hino R, Azuma R, Ito Y, Yamamoto Y, Suzuki K, Tsumura H, Suzuki S, Miyashita M, Tomori T, Arizono M, Tange G (2009) Insight into complex rupturing of the immature bending normal fault in the outer slope of the Japan Trench from aftershocks of the 2005 Sanriku earthquake (Mw = 7.0) located by ocean bottom seismometry. *Geochem Geophys Geosyst* 10:Q07018. <https://doi.org/10.1029/2009gc002415>
- Sagiya T (2004) Interplate coupling in the Kanto District, Central Japan, and the Boso Peninsula silent earthquake in May 1996. *Pure Appl Geophys* 161:2327–2342. <https://doi.org/10.1007/s00024-004-2566-6>
- Sato H, Hirata N, Koketsu K, Okaya D, Abe S, Kobayashi R, Matsubara M, Iwasaki T, Ito T, Ikawa T, Kawanaka T, Kasahara K, Harder S (2005) Earthquake source fault beneath Tokyo. *Science* 309:462–464
- Sato T, Higuchi H, Miyauchi T, Endo K, Tsumura N, Ito T, Noda A, Matsu'ura M (2016) The source model and recurrence interval of Genroku-type Kanto earthquakes estimated from paleo-shoreline data. *Earth Planets Space* 68:17. <https://doi.org/10.1186/s40623-016-0395-3>
- Sato T, Hasegawa S, Kono A, Shiobara H, Yagi T, Yamada T, Shinohara M, Usui N (2017) Detection of vertical motion during a slow-slip event off the Boso Peninsula, Japan, by ocean bottom pressure gauges. *Geophys Res Lett*. <https://doi.org/10.1002/2017GL072838>
- Sekiguchi S (2001) A new configuration and a seismic slab of the descending Philippine Sea plate revealed by seismic tomography. *Tectonophysics* 341:19–32. [https://doi.org/10.1016/S0040-1951\(01\)00182-2](https://doi.org/10.1016/S0040-1951(01)00182-2)
- Seno T, Maruyama S (1984) Paleogeographic reconstruction and origin of the Philippine Sea. *Tectonophysics* 102:53–84
- Shan S, Kao H, Obana K (2012) Structural characteristics of the northern Cascadia deformation front: preliminary result of SeaJade Experiment, presented at 2012 Fall Meeting, AGU, San Francisco, California, 3–7 Dec, Abstract T22D-04
- Shinohara M, Yamada T, Nakahigashi K, Sakai S, Mochizuki K, Uehira K, Ito Y, Azuma R, Kaiho Y, No T, Shiobara H, Hino R, Murai Y, Yakiwara H, Sato T, Machida Y, Shinbo T, Isse T, Miyamachi H, Obana K, Takahashi N, Kodaira S, Kaneda Y, Hirata K, Yoshikawa S, Obara K, Iwasaki T, Hirata K (2011) After-shock observation of the 2011 off the Pacific coast of Tohoku Earthquake by using ocean bottom seismometer network. *Earth Planets Space* 63:835–840. <https://doi.org/10.5047/eps.2011.05.020>
- Shinohara M, Machida Y, Yamada T, Nakahigashi K, Shinbo T, Mochizuki K, Murai Y, Hino R, Ito Y, Sato T, Shiobara H, Uehira K, Yakiwara H, Obana K, Takahashi N, Kodaira S, Hirata K, Tsumura H, Iwasaki T (2012) Precise aftershock distribution of the 2011 off the Pacific coast of Tohoku Earthquake revealed by an ocean-bottom seismometer network. *Earth Planets Space* 64:1137–1148. <https://doi.org/10.5047/eps.2012.09.003>
- Snoke J A (2003) FOCMEC: FOCal MECHANISM determinations. In: Lee W H K, Kanamori H, Jennings P C, Kisslinger C (eds) *International handbook of earthquake and engineering seismology*. Academic Press, San Diego, Chapter 85.12

- Spakman W, Nolet G (1988) Imaging algorithms, accuracy and resolution in delay time tomography. In: Vlarrr N et al (eds) *Mathematical geophysics*, D. Reidel, Norwell, pp 155–187
- Takahashi M (2006) Tectonic development of the Japanese islands controlled by Philippine Sea plate motion. *J Geogr* 115(1):116–123 **(in Japanese with English abstract)**
- Takemura M (1994) Aftershock activities for two days after the 1923 Kanto earthquake ( $M=7.9$ ) inferred from seismograms at Gifu Observatory. *Zisin* 46:439–455 **(in Japanese with English abstract)**
- Thurber CH, Eberhart-Phillips D (1999) Local earthquake tomography with flexible gridding. *Comput Geosci* 25(7):809–818
- Toda S, Stein RS, Kirby SH, Bozkurt SB (2008) A slab fragment wedged under Tokyo and its tectonic and seismic implications. *Nat Geosci* 1:771–776. <https://doi.org/10.1038/ngeo318>
- Tonegawa T, Hirahara K, Shibutani T (2005) Detailed structure of the upper mantle discontinuities around the Japan subduction zone imaged by receiver function analyses. *Earth Planets Space* 57:5–14
- Tonegawa T, Obana K, Yamamoto Y, Kodaira S, Wang K, Riedel M, Kao H, Spence G (2017) Fracture alignments in marine sediments off Vancouver Island from Ps splitting analysis. *Bull Seism Soc Am* 107(1):387–402. <https://doi.org/10.1785/0120160090>
- Tonegawa T, Obana K, Fujie G, Kodaira S (2018) Lateral variation of the uppermost oceanic plate in the outer-rise region of the Northwest Pacific Ocean inferred from Po-to-s converted waves. *Earth Planet Space* 70:106. <https://doi.org/10.1186/s40623-018-0880-y>
- Uchida N, Nakajima J, Hasegawa A, Matsuzawa T (2009) What controls inter-plate coupling?: evidence for abrupt change in coupling across a border between two overlying plates in the NE Japan subduction zone. *Earth Planet Sci Lett* 283:111–121
- Uchida N, Matsuzawa T, Nakajima J, Hasegawa A (2010) Subduction of a wedge-shaped Philippine Sea plate beneath Kanto, central Japan, estimated from converted waves and small repeating earthquakes. *J Geophys Res* 115:B07309. <https://doi.org/10.1029/2009JB006797>
- Ueno H, Hatakeyama S, Aketagawa T, Funasaki J, Hamada N (2002) Improvement of hypocenter determination procedures in the Japan Meteorological Agency. *Q J Seismol* 65:123–134 **(in Japanese with English abstract)**
- Wald DJ, Somerville PG (1995) Variable-slip rupture model of the great 1923 Kanto, Japan, earthquake—geodetic and body-wave-form analysis. *B Seismol Soc Am* 85:159–177
- Wu F, Okaya D, Sato H, Hirata N (2007) Interaction between two subducting plates under Tokyo and its possible effects on seismic hazards. *Geophys Res Lett* 34:L18301. <https://doi.org/10.1029/2007GL030763>
- Yamaji A (2000) The multiple inverse method applied to meso-scale faults in mid-Quaternary fore-arc sediments near the triple trench junction off central Japan. *J Struct Geol* 22:429–440
- Yamamoto Y, Takahashi T, Ishihara Y, Kaiho Y, Arai R, Obana K, Nakanishi A, Miura S, Kodaira S, Kaneda Y (2018) Modeling the geometry of plate boundary and seismic structure in the southern Ryukyu Trench subduction zone, Japan, using amphibious seismic observations. *J Geophys Res*. <https://doi.org/10.1002/2017JB015330>
- Yamauchi M, Hirahara K, Shibutani T (2003) High resolution receiver function imaging of the seismic velocity discontinuities in the crust and the uppermost mantle beneath southwest Japan. *Earth Planets Space* 55:59–64
- Zhang H, Thurber CH (2003) Double-difference tomography: the method and its application to the Hayward fault, California. *Bull Seismol Soc Am* 93:1875–1889
- Zhao D, Hasegawa A, Kanamori H (1992) Tomographic imaging of P and S wave velocity structure beneath northeastern Japan. *J Geophys Res* 97:19909–19928

### Publisher's Note

Springer Nature remains neutral with regard to jurisdictional claims in published maps and institutional affiliations.

Submit your manuscript to a SpringerOpen<sup>®</sup> journal and benefit from:

- Convenient online submission
- Rigorous peer review
- Open access: articles freely available online
- High visibility within the field
- Retaining the copyright to your article

Submit your next manuscript at ► [springeropen.com](https://www.springeropen.com)